catalysts

MDPI

Article

High Surface Area ZnO-Nanorods Catalyze the Clean Thermal Methane Oxidation to CO_2

Tanika Kessaratikoon [1], Sawarin Saengsaen [1], Silvano Del Gobbo [1,*], Valerio D'Elia [1,*] and Tawan Sooknoi [2]

[1] Department of Materials Science and Engineering, School of Molecular Science and Engineering, Vidyasirimedhi Institute of Science and Technology (VISTEC), Wangchan, Rayong 21210, Thailand
[2] Department of Chemistry, School of Science, King Mongkut's Institute of Technology Ladkrabang, Bangkok 10520, Thailand
* Correspondence: silvano.d@vistec.ac.th (S.D.G.); valerio.delia@vistec.ac.th (V.D.)

Abstract: ZnO nanostructures were synthesized by a combination of non-aqueous and aqueous sol-gel techniques to obtain morphologically different ZnO nanostructures, nanorods, and nanopyramids, featuring oxygen vacancies-rich exposed lattice faces and exhibiting different catalytic properties and activity. In particular, ZnO nanorods with high surface area (36 m^2/g) were obtained through a rapid, scalable, and convenient procedure. The materials were tested for complete methane oxidation as an important benchmark reaction that is sensitive to surface area and to the availability of oxygen vacancies. Simple ZnO nanorods derived from nanosized quantum dots showed the best catalytic performance that compared well to that of several literature-reported perovskites, mixed metal oxides, and single-metal oxides in terms of T_{50} (576 °C) and T_{90} (659 °C) temperatures. Such a result was attributed to their high surface-to-volume ratio enhancing the availability of catalytically active sites such as oxygen vacancies whose abundance further increased following catalytic application at high temperatures. The latter effect allowed us to maintain a nearly stable catalytic performance with over 90% conversion for 12 h at 700 °C despite sintering. This research shows that ZnO-based nanomaterials with a high surface area are viable alternatives to oxides of commonly applied (but of potentially limited availability) transition metals (La, Mn, Co, Ni) for the complete combustion of methane when working at moderate temperatures (600–700 °C).

Keywords: ZnO; nanorods; nanopyramids; clean methane combustion

Citation: Kessaratikoon, T.; Saengsaen, S.; Del Gobbo, S.; D'Elia, V.; Sooknoi, T. High Surface Area ZnO-Nanorods Catalyze the Clean Thermal Methane Oxidation to CO_2. *Catalysts* **2022**, *12*, 1533. https://doi.org/10.3390/catal12121533

Academic Editor: Leonarda Liotta

Received: 1 November 2022
Accepted: 24 November 2022
Published: 28 November 2022

1. Introduction

ZnO nanomaterials, in particular 1D structures, are extensively investigated for applications such as catalysis, and, in particular, photocatalysis [1–4], piezoelectric [5], antimicrobial [6], gas sensing [7], and optoelectronic applications such as LEDs [8], solar cells [9,10], and photodetectors [11]. In catalysis, ZnO-based materials were employed in systems used to promote the conversion of CO_2 to methanol [12], methanol steam reforming [13], biofuels synthesis [14], and, mainly, as photocatalysts for the photodegradation of organic dyes and pollutants [15,16], water splitting for hydrogen production [17], and other photo-promoted organic reactions [18]. The growing interest in ZnO-based materials is clearly due to the fact that zinc is a bio-compatible ubiquitous [19], abundant, and inexpensive metal that can be shaped in multiform morphologies [20,21]. Indeed, ZnO can be crystallized at the micro- and nanoscopic levels in a large variety of micro- and nanostructures that can be categorized as one-(1D), two-(2D), and three-dimensional (3D) materials. Given its wurtzite hexagonal structure, ZnO crystal tends to grow along the c-crystallographic axis giving rise to quasi-one-dimensional structures which are, by far, the most common and include nanorods [22,23], nanoneedles [24], nanowires [25], nanotubes [26], nanoribbons [27], nanocombs [28], and other structures [29]. Among such structures, nanometric ZnO nanorods (ZnO-NRs) can be obtained by convenient seeded-growth strategies [15,22]. They possess high electron transportability [30], high sensitivity

for sensing applications, [31] and higher thermal stability than ZnO nanoparticles [32]. It is, therefore, of high interest to expand the portfolio of applications of ZnO-NRs while improving their physico-chemical properties.

While many factors influence the catalytic activity of the active sites in ZnO materials such as the type of exposed crystallographic face [33,34] and the abundance of surface defects [35], it is obvious that the number of active sites is primarily strongly linked to the surface area of the material [36,37]. Therefore, it is fundamental to develop convenient and scalable methods to achieve ZnO-NRs with a satisfactory surface area. Lamentably, the surface area of free-standing ZnO-NRs prepared for various applications is generally very low and, very often, it does not exceed 10 m^2/g or it is close to such a value [38–40]. Cases where the surface area of ZnO-NRs approaches or slightly exceeds 20 m^2/g are relatively rare [41,42]. In a recent example, Chu, Cao et al. reported the synthesis of ZnO-NRs from zinc acetate with a very high surface area (55 $m^2 \cdot g^{-1}$); however, the synthetic procedure was quite lengthy (72 h) [43]. In the case of large-scale application of ZnO-NRs for catalytic applications, it would be convenient to develop an expedient and rapid synthesis of ZnO-NRs with a satisfactorily high surface area. In this work, we show that this can be achieved by suitable hydrothermal growth methods involving the use of pre-synthesized seeds that determine the final size of the nanorods.

As a test reaction for such ZnO-NRs, among a large variety of reactions catalyzed by metal oxides, we studied the selective catalytic combustion of methane as a process sensitive to the surface area [44–47] and other crucial surface features such as surface defects and oxygen vacancies [48,49]. In particular, such a process is highly attractive from the environmental standpoint as its implementation in place of the high-temperature flame-combustion of methane, which is pivotal in energy generation and hydrocarbons flaring, would avoid the formation of noxious gases such as CO and NO_x [50,51]. It would selectively lead to the formation of CO_2, which has a lower greenhouse gas potential than methane [52] and can be directly captured [53] and/or directly converted to chemicals [54–56] via increasingly efficient technologies.

In the last decades, several inorganic compounds have been reported for the catalytic combustion of methane. These include supported noble metals, perovskites, mixed metal oxides, metal oxides, and hexaaluminates [51,57–59]. The noble metal-based catalysts (e.g., containing palladium [60,61], palladium-gold [62,63], platinum [64], and rhodium [65]) are known for their low light-off temperatures and high catalytic activity for methane combustion and are suitable for operation at low temperature (350–500 °C). Despite this advantage, noble metals are rare, expensive, and prone to deactivation at high operating temperatures. Indeed, some operations involving methane combustion, such as combustion in gas turbines [57], are generally carried out at temperatures higher than 500 °C. Perovskites, mixed metal oxides, and some metal oxides are noble-metal-free compounds able to catalyze methane combustion at low to moderate temperatures [59]. Such systems include $LaMnO_3$ [66], $La_{0.9}Sr_{0.1}MnO_3$ [67], $LaCoO_3$ [44], $La_3Mn_2O_7$ [68], tridimensional macroporous $La_{0.6}Sr_{0.4}MnO_3$ [69], spinel-type oxides $NiCo_2O_4$ [48] and $Ni_{0.5}Co_{2.5}O_4$ [70], and mixed metal oxides such as $Ce_{0.5}Ni_{0.5}O_2$ [71], manganese-cobalt oxides [72], Ce/Co_3O_4 [73], and MnOx(0.13)–NiO [74]. Among single-metal oxides, manganese oxide has shown high activity at low to moderate reaction temperatures [75,76]. Nevertheless, it should be taken into account that metals such as nickel and cobalt are much more expensive than zinc with a price per metric ton that is, respectively, seven and twenty times higher than zinc. Additionally, cobalt is a critically endangered metal in terms of future supply [77]. At the same time, reserves of high-quality manganese ores are extremely geographically restricted [77,78], and, whereas the current price of manganese is just slightly higher than zinc, its demand is expected to increase enormously for use in batteries [79,80]. Therefore, it is worth investigating zinc as a ubiquitously available "workhorse" metal for applications on a large scale such as methane combustion in gas turbines or industrial flaring.

Interestingly, there has been scarce attention towards ZnO application in methane combustion although previous theoretical work has shown that methane can be activated on

ZnO and react with dioxygen on such surfaces [81]. ZnO-NRs on monolith substrate have been used as support for $La_{0.8}Sr_{0.2}CoO_3$ in the thermocatalytic and solar-drive oxidation of methane; however, to the best of our knowledge, the performance of the unfunctionalized ZnO-NRs was not reported [82]. Interestingly, ZnO-NRs arrays were reported to be inactive in propane combustion up to a temperature of 600 °C [83].

In this work, we investigated the catalytic activity towards the selective combustion of methane of three nanostructured ZnO-based catalysts: ZnO-(Q)NRs (i.e., ZnO nanorods grown by hydrothermal synthesis from ZnO quantum dot seeds (ZnO-QDs)), ZnO-(Py)NRs (i.e., ZnO nanorods grown by hydrothermal synthesis from ZnO nanopyramids (ZnO-NPys)) and ZnO-NPys synthesized by non-hydrolytic sol-gel. Additionally, commercial ZnO was studied as reference material. While ZnO-(Py)NRs and ZnO-NPys presented a higher density of surface-active sites than ZnO-(Q)NRs, we show here that ZnO-(Q)NRs with a high surface area could be obtained via a facile and rapid approach leading to a more efficient material for the selective oxidation of methane than the other ZnO-nanomaterials. For ZnO-(Q)NRs, the T_{50} and T_{90} temperatures (temperature required for the conversion of 50% and 90% of methane in the feed, respectively) compared well to those of various perovskite materials, and the catalytic performance did not change significantly after 12 h time-on-stream (TOS).

2. Results

ZnO-NRs can be synthesized with precise control over the size (diameter) using pre-synthesized nanoparticles to seed and direct the growth of the nanorods [22,84]. In recent examples, we synthesized ZnO-NRs in 12 h using different amounts of zinc oxide nanopyramid and nanoparticle seeds providing nanorods with different average lengths (~1000 and ~200 nm, respectively) [15,22]. However, the effect of the precursor used and of the synthetic parameters on the surface area of ZnO-NRs were not investigated. In this work, given the importance of optimizing the latter parameter in heterogeneous catalysis, two size tiers of ZnO-NRs were prepared using two different kinds of seeds (ZnO quantum dots (QD) and nanopyramids (NPy)) by varying the growth time. According to such an approach, we obtained ZnO-(Q)NRs with smaller diameter and length than ZnO-(Py)NRs obtained from ZnO-NPys seeds. In particular ZnO-(Q)NRs synthesized within just 1 h showed the smallest size and the highest surface area and pore volume. The characterization of the synthesized materials was carried out by SEM for statistical analysis of the images, XRD for morphological analysis, BET analysis for the determination of the surface area, and H_2 temperature programmed reduction (H_2-TPR), O_2 temperature programmed desorption (O_2-TPD), photoluminescence (PL), and X-Ray photoelectron spectroscopy (XPS) for defects and vacancies characterization.

2.1. SEM Characterization

The SEM images of ZnO-NPys seeds are shown in Figure S1a. These seeds are represented by nano-sized pyramids with hexagonal bases with an average base size of about 100 nm and a height of about 70 nm. The TEM image of the ZnO-QDs is provided in Figure S2a; the average size distribution of the QD was centered at 4.7 nm (Figure S2b). The images in Figure 1 and the results in Table 1 show that a preparation time of 1 h led to the formation of tiny ZnO-(Q)NRs with a length of 230 nm and a diameter of about 25 nm. For the ZnO-(Q)NRs samples, the time of synthesis had a significant effect on size. An increase in the preparation time over 1 h led to a significant increase in size (length and diameter) in all cases (Table 1). Statistical distributions of the dimensions are illustrated in Figure S3. Indeed, ZnO-(Q)NRs that were prepared with a time longer than 1 h had an average length of at least 500–700 nm with bimodal (2 h) or even trimodal (12 h) distributions and average diameters above 50 nm. Given the absence of residual ZnO-QD seeds even after just 1 h in the ZnO-(Q)NRs sample (Figure 1a), the formation of larger ZnO-NRs under longer preparation times could be attributed to the occurrence of Ostwald ripening leading to larger nanostructures by consumption of smaller ZnO-NRs.

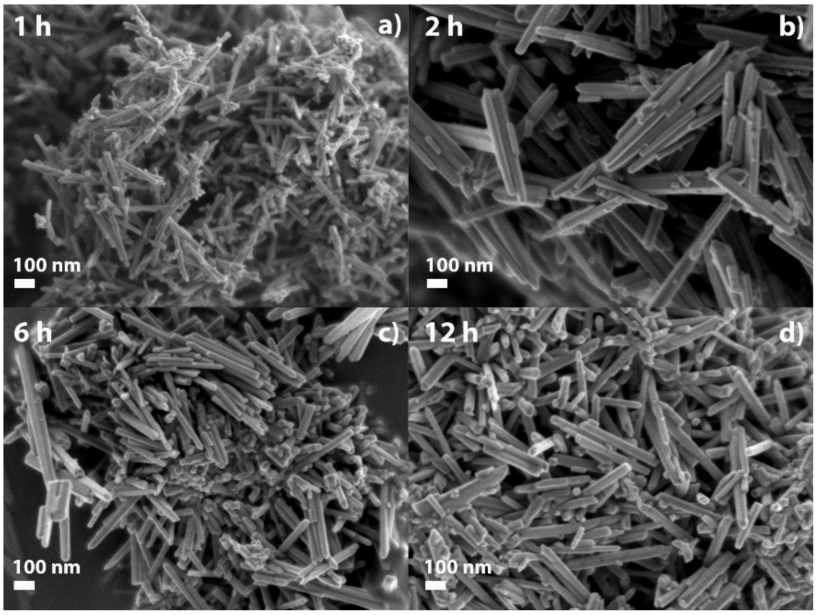

Figure 1. SEM images of ZnO-(Q)NRs synthesized for (**a**) 1, (**b**) 2, (**c**) 6, and (**d**) 12 h.

Table 1. Dimensions of the ZnO-(Q)NRs in Figure 1 and ZnO-(Py)NRs in Figure 2.

Material	Synthesis Time (h)	Length (nm)	Diameter (nm)
ZnO-(Q)NRs	1	230 ± 69	25 ± 1
	2	574 ± 17, (825 ± 5)	65 ± 1
	6	679 ± 33	58 ± 2
	12	559 ± 3, (920 ± 6) [a], (1192 ± 7) [a]	52 ± 2, (76 ± 1) [a]
ZnO-(Py)NRs	1	885 ± 11	98 ± 4
	12	1106 ± 25	94 ± 3

[a] The values in brackets refer to minor components within multimodal distributions.

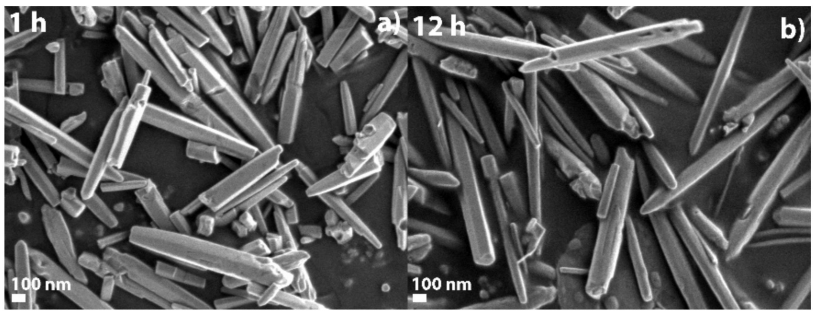

Figure 2. SEM images of ZnO-(Py)NRs synthesized for (**a**) 1 and (**b**) 12 h.

From Table 1, the ZnO-(Py)NRs (See SEM images in Figure 2) displayed similar sizes in terms of length and diameter after growth for 1 h and 12 h. Size distributions are shown in Figure S4. The SEM images in Figure 2 show that the NPy precursors were consumed within the first hour of the synthesis. Therefore, also in this case, the small difference in size, mainly in length, between the ZnO-(Py)NRs prepared in 1 h and in 12 h can be explained in terms of ripening, which led to the higher energy surface such as $\{10\bar{1}0\}$ to redissolve in favor of a lower energy surface such as $\{000\bar{1}\}$ [85,86], resulting in the growth of the crystal along the c-axis rather than in other crystallographic directions.

2.2. BET Characterization

The BET surface area values measured for the ZnO-(Q)NRs and ZnO-(Py)NRs samples along with ZnO-NPys and commercial ZnO (ZnO-C), as reference materials, are shown in

Table 2. As expected, the largest surface area was obtained for the sample with the smaller size, i.e., the ZnO-(Q)NRs prepared in 1 h (36 m^2/g). The surface area for the ZnO-(Q)NRs prepared with longer times was always in the 15–17 m^2/g range due to the presence of a main length distribution around 560–700 nm and similar diameter (50–65 nm, Table 1), in all cases. The ZnO-(Py)NRs had a smaller surface area, of just 6 m^2/g, than all ZnO-(Q)NRs due to the consistently larger average size (close to 1 µm in length and 100 nm in diameter, Table 1) than all ZnO-(Q)NRs. This surface area was just slightly higher than for ZnO-C without a well-defined morphology (5 m^2/g). The ZnO-NPys displayed a surface area of 14 m^2/g. All materials displayed N_2 sorption isotherms of type II (Figures S5 and S6) relative to nonporous materials indicating that the low observed porosity was exclusively due to the voids between the particles. Based on the higher surface area value, for the remainder of this work we will focus on ZnO-(Q)NRs prepared in 1 h. For comparison, ZnO-(Py)NRs prepared in 1 h will be considered. Finally, ZnO-NPys and ZnO-C will be studied as reference materials.

Table 2. Effect of synthesis time on BET surface area.

Material	Synthesis Time (h)	BET Surface Area (m^2/g)	Pore Volume (cm^3/g)
ZnO-(Q)NRs	1	36	0.47
	2	15	0.089
	6	17	0.12
	12	17	0.14
ZnO-(Py)NRs	1	6	0.033
	12	6	0.033
ZnO-NPys	-	14	0.21
ZnO-C	-	5	0.025

2.3. X-ray Diffraction Characterization

The powder XRD patterns of pristine ZnO-(Q)NRs, ZnO-(Py)NRs, ZnO-NPys, and the commercial ZnO (ZnO-C) used as a reference are shown in Figure 3. Based on the powder XRD patterns, all nanostructures possess well-defined wurtzite crystalline structures with the three intense main peaks related to the (100), (002), and (101) reflections in evidence. The sole difference observable among the four samples is the intensity ratio between the quoted peaks which is due to the dimensionality and the preferential orientation of the nanostructures. In particular, for ZnO-(Q)NRs and ZnO-(Py)NRs, one observes a higher relative intensity of the (002) peak in comparison with (100) and (101) due to the morphology of the nanorod developing along the c-axis, i.e., by the {0001} planes family. This is particularly evident for the ZnO-(Q)NRs, whereas ZnO-(Py)NRs feature also an intense (101) peak relative to lateral planes of the rod given their larger diameter. It is also interesting to observe that, in the ZnO-(Q)NRs XRD pattern, the peaks of the (100) and (101) reflections are wider than the (002) peak, which is not affected by the reduced dimensionality, as expected, according to the Debye–Scherrer relation.

2.4. H_2-TPR Characterization

The total combustion of methane generally follows a Mars–van Krevelen mechanism [57,82] with the transfer of active oxygen species from the surface of the catalyst to the substrate. The surface oxygen species are subsequently restored by the oxygen molecules present in the feed. At lower temperatures, such active surface oxygen species are represented by relatively weakly chemisorbed species adsorbed at the oxygen vacancies of the metal oxide, while, at higher temperatures, the surface and bulk lattice oxygen may also be involved in the process [87,88]. It is, therefore, attractive to investigate the H_2-TPR (TPR: temperature programmed reduction) of the materials applied in this study as a way to estimate oxygen mobility [47].

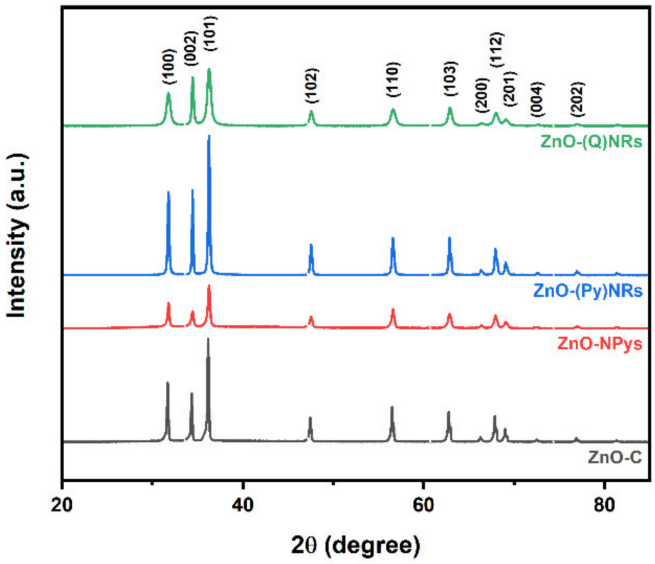

Figure 3. XRD patterns of pristine ZnO-(Q)NRs, ZnO-(Py)NRs, ZnO-NPys, and ZnO-C.

While it should be noted that ZnO is generally a non-reducible oxide [89], as confirmed by H_2-TPR studies of several ZnO materials [90,91], reduction peaks in the 400–550 °C temperature range were observed in some studies of ZnO and attributed to the release of surface oxygen atoms, likely chemisorbed species, leading to the formation of oxygen vacancies on the oxide surface [92,93]. The H_2-TPR profiles in Figure 4 show, indeed, the presence of weak reduction signals in the 450–600 °C range. The position of such signals slightly changed from case to case as different morphologies present different surface oxygen atoms on the lattice planes exposed. ZnO-NPys showed a higher volume of hydrogen consumed, and the reduction signal was shifted at slightly lower temperatures (450 °C) compared to the other materials in Figure 4. Such behavior could be attributed to the higher surface energy of the lattice planes exposed $\{000\bar{1}\}$ (base) and $\{10\bar{1}1\}$ (pyramid faces) [94]. Therefore, ZnO-NPys showed a higher tendency to generate active oxygen species under reductive conditions followed by ZnO-C but with a reduction signal shifted at a much higher temperature (~600 °C) as observed elsewhere [95]. Both ZnO-NRs materials showed a much lower reduction signal at 500 °C when compared to ZnO-NPys, showing a lower propensity to generate oxygen vacancies under reductive conditions than the latter material. Importantly, these data should be complemented by a study on the ability of the ZnO-nanomaterials to interact with oxygen through preexisting vacancies, as discussed below, by O_2-TPD and XPS investigations. Finally, both kinds of ZnO-NRs, as well as ZnO-NPys, showed a larger and broader reduction peak at high temperatures starting from about 600 °C for the ZnO-NRs and 700 °C for ZnO-NPys, which may indicate the reduction of zinc ions from the lattice of the materials [96]. Such signals are not observed for ZnO-C in line with its reported non-reducibility. To note, such reduction peaks appear at higher temperatures than observed for the inception of the methane combustion curves (*vide infra*), indicating that such lattice oxygen is not, at least initially, involved in the oxidation process.

2.5. O_2-TPD Characterization

The O_2-temperature programmed desorption (O_2-TPD) is a crucial way to investigate the oxygen mobility of an oxide material and its ability to provide oxygen atoms for the oxidation of methane. Additionally, it provides information on which kind of oxygen atoms are involved in the oxidation process [88]. The O_2-TPD profiles of the investigated ZnO materials are provided in Figure 5a in the 100–600 °C range. To avoid the interference of the surface dihydroxylation typically occurring for metal oxides at elevated temperatures [97], all materials were pretreated up to 550 °C under an inert atmosphere. However, this treatment led to the decomposition of the ZnO-NPys that were, therefore,

not included in this study. All materials in Figure 5a showed an O_2 desorption signal in the 300–500 °C range, albeit differing in intensity from case to case. For ZnO-(Q)NRs and ZnO-(Py)NRs, the O_2-TPD peak was clearly the result of the overlap of at least two components; the first, occurring at 350–400 °C, is attributed to the desorption of weakly coordinated superficial oxygen adsorbed on oxygen vacancies (O_{ads}) [98]; the second (mostly occurring in the 400–500 °C range) is attributed to mobile low-coordination superficial lattice oxygen [99]. However, the O_2-TPD signal of ZnO-C consists exclusively of surface lattice species (400–450 °C range), likely indicating a less defective material. In general, in catalytic studies on methane combustions, the oxygen desorbed below 500–600 °C, depending on the kind of material, is indicated as α-O_2, which is made of the contribution of adsorbed oxygen on oxygen vacancies and mobile surface lattice. Such oxygen species are responsible for methane conversion at low to moderate temperatures [49,88,100]. Indeed, the onset of the methane light-curves in this study (*vide infra*) is found at 400 °C, which is in line with the participation of the α-O_2 species observed in Figure 5 in the reaction. At temperatures above 600 °C, the bulk oxygen atoms of the materials lattice (O_{latt}) are assumed to take part in the combustion process [101].

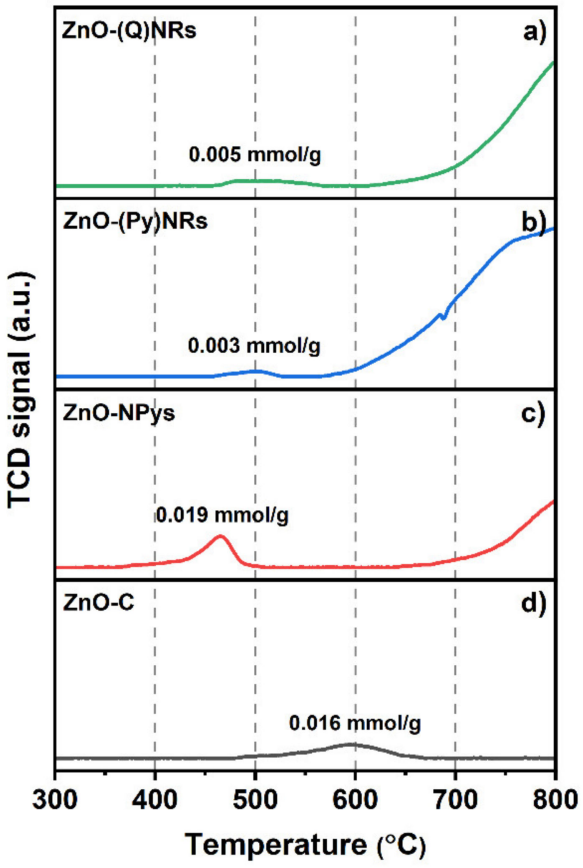

Figure 4. H_2 Temperature-programmed reduction curves of pristine (**a**) ZnO-(Q)NRs, (**b**) ZnO-(Py)NRs, (**c**) ZnO-NPys, and (**d**) ZnO-C.

Importantly, according to the O_2-TPD profiles shown in Figure 5a, ZnO-(Q)NRs carried the largest amount of α-O_2, which is in line with its higher surface area compared to the other materials. Nevertheless, the surface area-normalized volume of desorbed O_2 (Figure 5b) shows that there is a higher density of active sites for oxygen desorption on ZnO-(Py)NRs when compared to ZnO-(Q)NRs while ZnO-C showed the lowest density of such catalytically relevant sites. These aspects are complemented by the PL and XPS studies shown below.

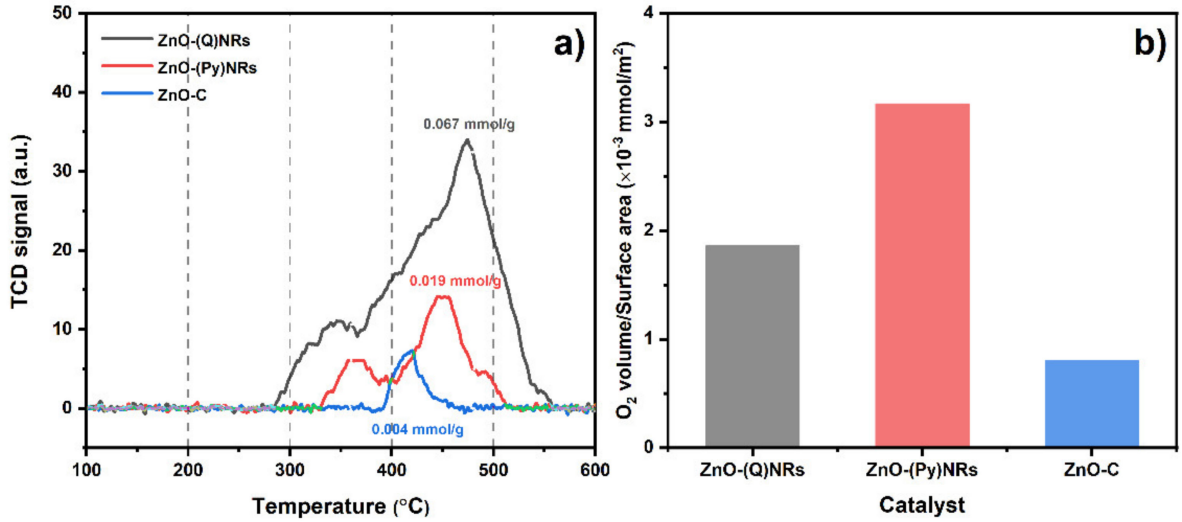

Figure 5. (**a**) O_2-TPD profiles for as-synthesized ZnO-(Q)NRs, ZnO-(Py)NRs, and ZnO-C. (**b**) Surface area-normalized volume of desorbed O_2.

2.6. Photoluminescence Spectroscopy Characterization

Photoluminescence spectroscopy (PL) of semiconductor nanostructures is a widely used technique to probe the amount and the kind of defects present in the materials [15,102,103]. As recommended by Brik et al. in a recent editorial, the deconvolution of the spectral components has been carried out in the energy domain [104]. Besides a sharp emission band at 3.2–3.3 eV relative to the direct band gap transition (near band edge UV emission), the PL spectra of ZnO nanomaterials are characterized by a more complex emission in the 1.5–2.8 eV nm region relative to the amount and type of defects present in the nanostructure [105,106]. In general, a green emission is attributed to single-charged oxygen vacancies, a yellow emission to double-charged oxygen vacancies, and an orange-red emission to excess oxygen on the surface defects (O_{ads}) and/or zinc vacancies [15,102,105,106]. All these defects can be conductive to enhancing the catalytic performance of the metal oxides in methane oxidation: single- and double-charged vacancies can bind oxygen in the form of superoxide [107,108], which is an active species in methane oxidation [88], while the O_{ads} component represents a variety of oxygen species already adsorbed on oxygen vacancies, including the superoxide [109,110], that play a crucial role in methane oxidation [74,111].

The PL spectra of the as-synthesized catalytic materials and ZnO-C are shown in Figure 6a–d. The PL spectra of the ZnO-NRs materials (ZnO-(Q)NRs and ZnO-(Py)NRs) are dominated by the defects-related emission bands that are constituted by the three components described above (Figure 6a,b). It is necessary to stress that the accuracy of the deconvolution at high wavelengths is partially affected by the detector cutoff at 1.5 eV; however, it can still usefully serve in the qualitative analysis of defects in ZnO nanostructures. For ZnO-(Q)NRs, the main component of the defects-related emission was represented by a peak at 1.74 eV (712 nm) relative to $O_{ads,}$ indicating the availability of abundant surface species for methane oxidation. For ZnO-(Py)NRs, presenting the most intense defect-related emission of all samples, the main component in the defect-related emission was represented by the band at 2.02 eV (614 nm) relative to double-charged oxygen vacancies while the component relative to O_{ads} was lower in intensity. When compared to the ZnO-NRs materials, the PL spectra of ZnO-NPys and ZnO-C showed a much lower intensity of the defect-related emission relative to near-band edge transition at 3.2–3.3 eV. For ZnO-NPys, the main component relative to O_{ads} centered at 1.82 eV (683 nm) was blue-shifted compared to the previously described ZnO-NRs materials (Figure 6c). The PL spectrum of ZnO-C was very different from the other materials since it was mainly centered in the green region of single-charged oxygen vacancies at 2.41 eV (514 nm) and also featured other weaker components (Figure 6d). Apart from the obvious structural

differences, the PL spectra show that the ZnO-NRs-based materials (ZnO-(Q)NRs and ZnO-(Py)NRs) displayed a much more defective structure than ZnO-NPys and ZnO-C with abundant O_{ads} and double-charged oxygen vacancies that can enhance methane oxidation as previously discussed.

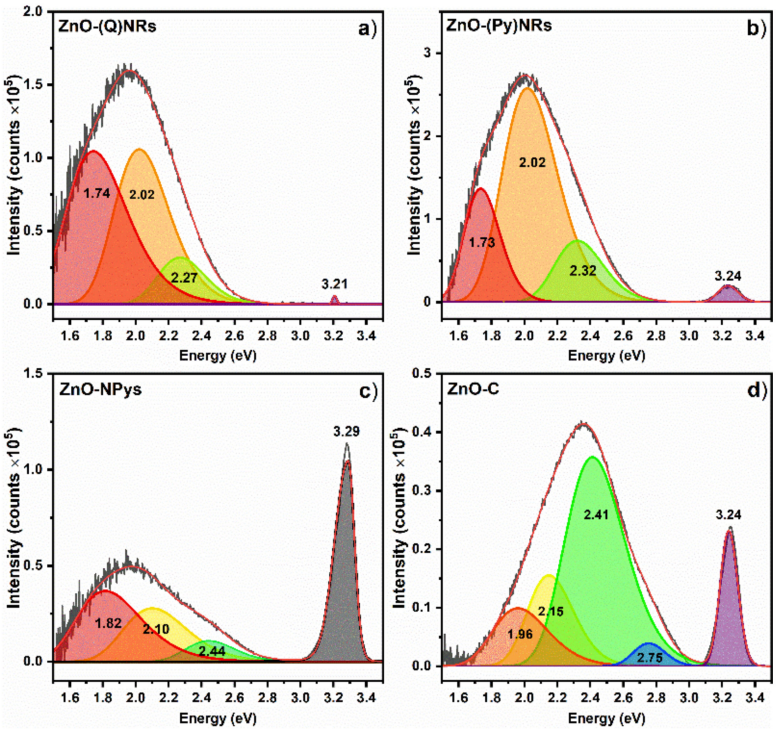

Figure 6. Photoluminescence spectra of pristine (**a**) ZnO-(Q)NRs, (**b**) ZnO-(Py)NRs, (**c**) ZnO-NPys, and (**d**) ZnO-C. Excitation wavelength: 300 nm.

2.7. XPS Investigation

XPS spectroscopy was used to investigate the surface features of ZnO-(Q)NRs, ZnO-(Py)NRs, ZnO-NPys, and ZnO-C. The XPS spectra of pristine ZnO-(Q)NRs, ZnO-(Py)NRs, ZnO-NPys, and ZnO-C samples are shown in Figure 7 for the multicomponent O 1s peak and the Zn 2p peaks, with the latter split by the spin–orbit interaction into $2p_{3/2}$ and $2p_{1/2}$ signals. The chemical shifts of each O1s and Zn 2p synthetic component are reported in Table S1. For Zn 2p, the Zn $2p_{3/2}$ and Zn $2p_{1/2}$ peaks were detected for all samples at about 1021.6–1022.0 eV and at about 1044.7–1045.1 eV, respectively, with a typical separation of 23.1 eV attributed to Zn^{2+} ions [15]. For O 1s, three spectral components are identified and denoted as O_I, O_{II}, and O_{III}. The O_I component (generally observed at 530.0–530.5 eV) is attributed to bulk lattice oxygen atoms. The O_{II} component (generally observed at 531.5–531.9 eV) is attributed to oxygen atoms in an oxygen-vacant environment while O_{III} (generally observed at 532.5–533.4 eV) is attributed to surface –OH groups and adsorbed oxygen species [15,112]. In several studies on total methane combustion, the ratio between O_{ads}, as identified by XPS, and O_I (O 1s component relative to lattice oxygen) has been used as a proxy for catalytic activity as this parameter provides information on the availability of adsorbed oxygen species, such as superoxide, which serve in methane activation [45,113,114]. For those studies, however, no O 1s component relative to oxygen vacancies, which generally is an important component of O 1s in metal oxides [37], was deconvoluted.

In our case, it is worth considering both components O_{II} and O_{III} as the former refers to oxygen vacancies that are available, during reaction, for the formation of superoxide from molecular oxygen [48], while the latter provides an estimation of the amount of O_{ads} on the catalyst surface. Therefore, the weights of the O_I, O_{II}, and O_{III} components relative to total oxygen ($O_{tot} = \Sigma O_N$, N = I–III) are displayed in Table 3. It is possible to

observe that nearly all samples (ZnO-(Q)NRs, ZnO-NPys, and ZnO-C) presented very similar proportions of each component as indicated by the nearly identical O 1s spectra in Figure 7. As a consequence, such materials also presented similar combined abundances of (O_{II} + O_{III}) species as a fraction of the total. However, for ZnO-(Py)NRs, a higher proportion of oxygen vacancies was identified compared to the other samples (Table 3) due to the intense O_{II} component in Figure 7c. This result is in agreement with the PL spectra in Figure 6 showing a very strong component relative to (double-charged) oxygen vacancies for ZnO-(Py)NRs (Figure 6b). On the other hand, differently from what was observed from PL (Figure 6a), ZnO-(Q)NRs showed a ratio of vacancies to total oxygen similar to that of ZnO-C and ZnO-NPys. However, the two different techniques (PL and XPS) may not be directly comparable as they differ in the degree of penetration in the sample.

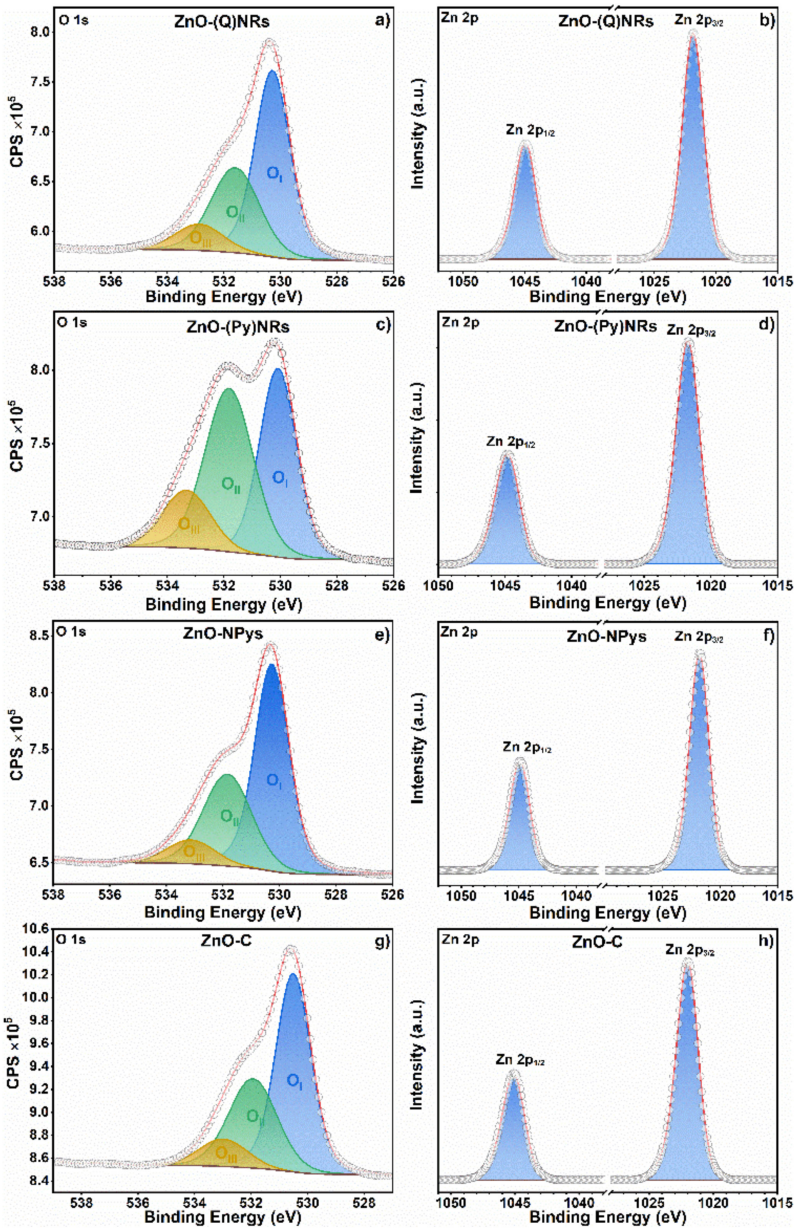

Figure 7. High-resolution XPS spectra of pristine (**a**,**b**) ZnO-(Q)NRs, (**c**,**d**) ZnO-(Py)NRs, (**e**,**f**) ZnO-NPys and (**g**,**h**) ZnO-C samples in the O 1s and background-subtracted Zn 2p spectral regions.

2.8. Morphological Characterization of Spent Catalysts

A series of post-reaction investigations were carried out for the spent catalysts in order to study the effect of the reaction temperature on morphology. For the sake of providing

a concise overview, only the images for the catalyst with the lowest T_{50} and T_{90} values, ZnO-(Q)NRs (*vide infra* for catalytic results), are given in this section, whereas the images relative to the other materials are given in the Supporting Information.

Table 3. Intensity ratios of normalized O 1s components relative to the total oxygen area (O_{tot}).

Catalyst	O_{III}/O_{tot}	O_{II}/O_{tot}	O_I/O_{tot}	$(O_{III}+O_{II})/O_{tot}$
ZnO-(Q)NRs	0.10	0.33	0.57	0.43
ZnO-(Py)NRs	0.15	0.45	0.40	0.60
ZnO-NPys	0.08	0.34	0.58	0.42
ZnO-C	0.10	0.33	0.57	0.43

SEM images of the ZnO-(Q)NRs sample retrieved after the prolonged exposure (12 h) to the reaction conditions in time-on-stream (TOS) experiments are given in Figure 8. The sample used at 500 °C showed an alteration of the morphology of the surface of the nanorods, appearing as a smoothing of the edges of the hexagonal pencil-like shape of the pristine particles (Figure 8b). This effect increased by increasing the temperature leading to partially sintered NRs at 600 °C (Figure 8c). A massive melting was observed at 700 °C, with the formation of larger structures from the initial NRs (Figure 8d). Sintering could also be observed for ZnO-NPys (Figure S1) and for ZnO-C (Figure S7, sample retrieved after light-off investigation in the 400–700 °C range). In the case of ZnO-NPys, the melting and sintering were apparent already at 500 °C, and there was no strong difference between the samples retrieved after TOS reaction at 500 or 700 °C. This strong thermal degradation took place because of the quasi-0D morphology of ZnO-NPys that favors the sintering of the nanostructures. The occurrence of sintering was less evident for ZnO-(Py)NRs (Figure S8), and the high temperatures did not cause any strong change in the ZnO-(Py)NRs morphology. In this case, the large size and the possibility to arrange in entangled networks made the ZnO-(Py)NRs much more resistant to high temperatures than the other materials.

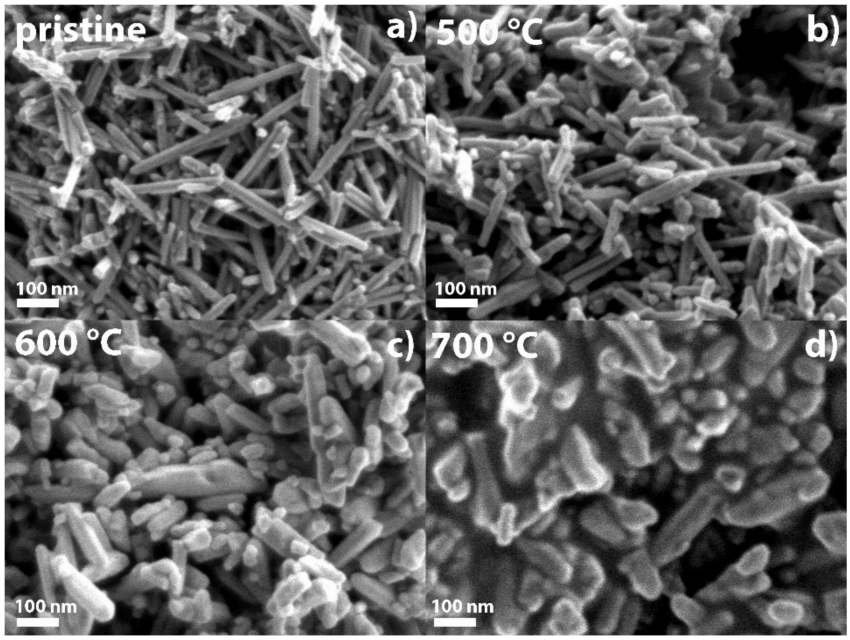

Figure 8. SEM images of ZnO-(Q)NRs (**a**) pristine and after use in time on stream (TOS) reactions at (**b**) 500 °C, (**c**) 600 °C, and (**d**) 700 °C.

The thermal treatment did not lead to large changes in the XRD patterns for ZnO-(Q)NRs except for the presence of traces of SiO_2, which was used as a diluent in the reactor and could not be removed completely by sieving (Figure 9). Additionally, for the other ZnO nanostructures, the bulk structure, which gives the largest contribution to the XRD

diffraction, remained basically unchanged after the thermal exposure (Figures S9–S11). Nevertheless, for ZnO-(Q)NRs, an evident change in the relative intensities of the (100), (002) and (101) diffraction peaks can be noted with the intensity of the (002) diffraction peak decreasing relatively to the (100) and (101) peaks after use. This is due to a shortening of the NRs after their use due to sintering as observed by SEM. The same effect was not observed for ZnO-(Py)NRs due to limited sintering.

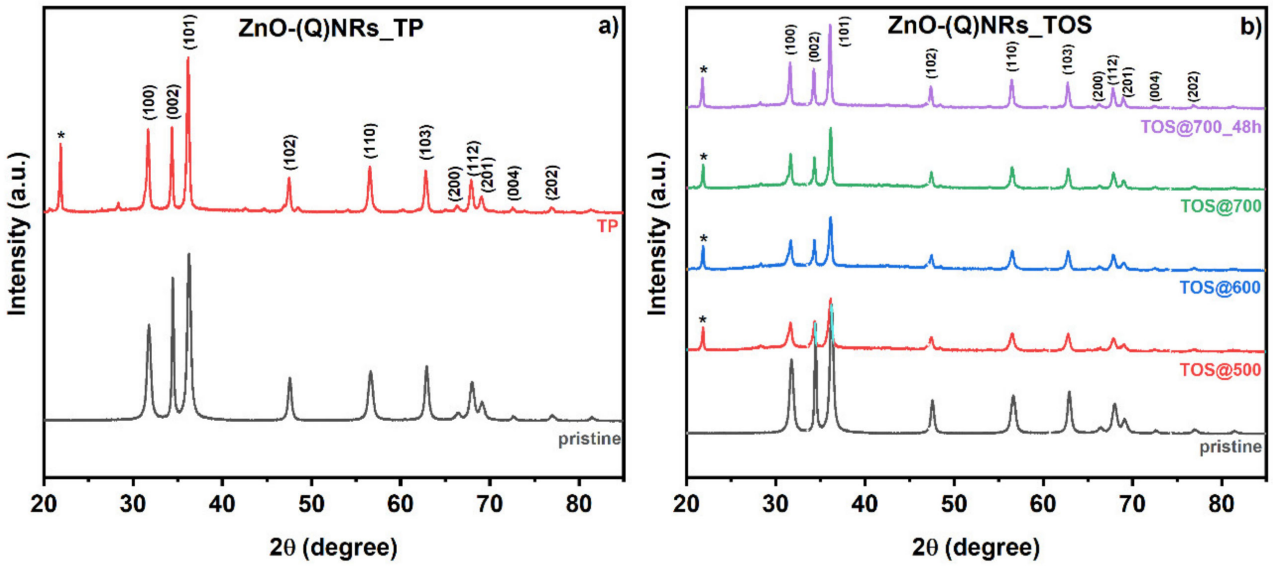

Figure 9. XRD patterns of ZnO-(Q)NRs (**a**) pristine and after use from 400 °C to 700 °C temperature range (TP), (**b**) pristine and after use at 500 °C, 600 °C, and 700 °C in time on stream (TOS) reactions. The diffraction signal of the traces of quartz silica used as a dilutant is labeled with (*).

The variation of surface area of the ZnO-(Q)NRs after use in the 400–700 °C temperature range for the light-off curve by temperature program (TP) and the TOS reactions at various temperatures is reported in Figure 10 along with the variation of the surface area of the other ZnO-nanomaterials after temperature program investigation. It is evident that treatment at high temperatures led to a progressive sintering of the nanostructures used in this work, which is observed for all materials as confirmed by the SEM investigation. While for ZnO-(Q)NRs, the reduction of surface area after use in the light-off study is proportionally larger than for other materials such as ZnO-(Py)NRs and ZnO-C, it still retained a surface area similar to that of pristine ZnO-NPys. The sample retrieved after TOS reaction for 12 h at 500 °C showed a surface area of about 12 $m^2 \cdot g^{-1}$, similar to that observed after the light-off investigation. Increasing the temperature of the TOS reaction led to a further reduction of surface area after 12 h, which was just about 5 $m^2 \cdot g^{-1}$ after 12 h at 700 °C. At such temperatures, extending the treatment to 48 h resulted in only a small further reduction of surface area to about 5 $m^2 \cdot g^{-1}$ (Exact values for all samples are detailed in Table S2).

2.9. Catalytic Methane Combustion

All ZnO catalysts (ZnO-(Q)NRs, ZnO-(Py)NRs, ZnO-NPys, and ZnO-C) were tested for the combustion reaction of methane utilizing a gas mixture comprising 1% CH_4 and 99% synthetic air with a total flow rate of 100 mL/min and gas hourly space velocity (GHSV) of 30,000 $mL \cdot g_{cat}^{-1} \cdot h^{-1}$. All reactions generally afforded CO_2 selectively, and CO was observed only in trace amounts. An initial investigation of catalytic activity was carried out in the 400 °C to 700 °C temperature range with an increment of 50 °C (See light-off curves in Figure S12). The contribution to the methane conversion by the solid dilutant SiO_2 was excluded by running a blank reaction by filling the reactor only with SiO_2, virtually resulting in insignificant conversion, as shown in Figure S13. As expected on

the basis of the higher surface area, the most active catalyst was found to be ZnO-(Q)NRs, featuring the highest conversion at 650 °C and the lowest T_{50} (576 °C) and T_{90} (659 °C) temperature values (Table 4). Additionally, ZnO-(Q)NRs led to the virtually complete combustion of methane at 700 °C with about 97 % conversion. Commercially available zinc oxide (ZnO-C) did not reach full methane conversion below 700 °C. Considering the methane conversion at 650 °C as a parameter, the activity of the catalysts decreased in the order ZnO-(Q)NRs > ZnO-(Py)NRs ~ ZnO-NPys >> ZnO-C.

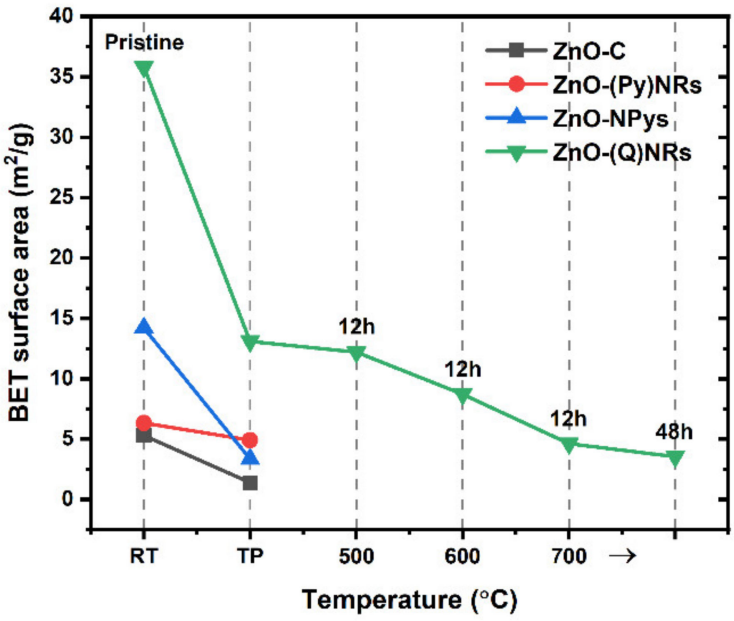

Figure 10. Variation of the surface area of ZnO catalysts at pristine, after temperature program (TP) from 400 °C to 700 °C, and after time on stream (TOS) reactions at 500 °C, 600 °C, and 700 °C.

Table 4. T_{50}, T_{90} temperature values and conversion at 650 °C for the ZnO-based nanomaterials.

Catalyst	T_{50} (°C)	T_{90} (°C)	Conv. (%) (at 650 °C)	Surface Area ($m^2 \cdot g^{-1}$)
ZnO-(Q)NRs	576	659	88	36
ZnO-(Py)NRs	609	689	74	6
ZnO-NPys	615	696	71	14
ZnO-C	665	-	41	5

Given the tendency of the ZnO-nanomaterials to sinter as discussed above, the stability of the catalytic performance at high temperatures was studied by carrying out time on-stream reactions (TOS) at 500 °C, 600 °C, and 700 °C for 12 h using the three most active catalysts, ZnO-(Q)NRs, ZnO-(Py)NRs, and ZnO-NPys (See plots in Figure 11 for ZnO-(Q)NRs and Figures S14 and S15 for ZnO-(Py)NRs and ZnO-NPys, respectively). To note, such kind of investigation is relatively seldom carried out for methane combustion catalysts [115,116].

At 500 °C (Figure 11a), the conversion of methane of ZnO-(Q)NRs remained basically stable at 12 % over a period of 12 h. At 600 °C (Figure 11b), there was a slight decline of conversion from 63 % to 54 % over six hours followed by a less evident linear decline to 51% at the twelfth hour. The highest conversion of 99% was afforded at 700 °C (Figure 11c), which only marginally decreased to 92 % after 12 h on stream, showing a relatively high stability of the catalytic performance (Figure 11d).

The TOS reactions over ZnO-(Py)NRs and ZnO-NPys showed a similar trend of methane conversion compared to ZnO-(Q)NRs, albeit with lower catalytic activity. The results are presented in Figures S14 and S15, respectively. ZnO-(Py)NRs afforded a high initial methane conversion of 97% at 700 °C, while at the same temperature, ZnO-NPys

afforded 87 % conversion. Over 12 h, the conversion of methane declined to 78 % for both catalysts. Overall, among the three catalysts, ZnO-(Py)NRs showed the most significant decrease in conversion after 12 h TOS reaction at 700 °C (20%) followed by ZnO-NPys (10%) and finally ZnO-(Q)NRs (7.6%).

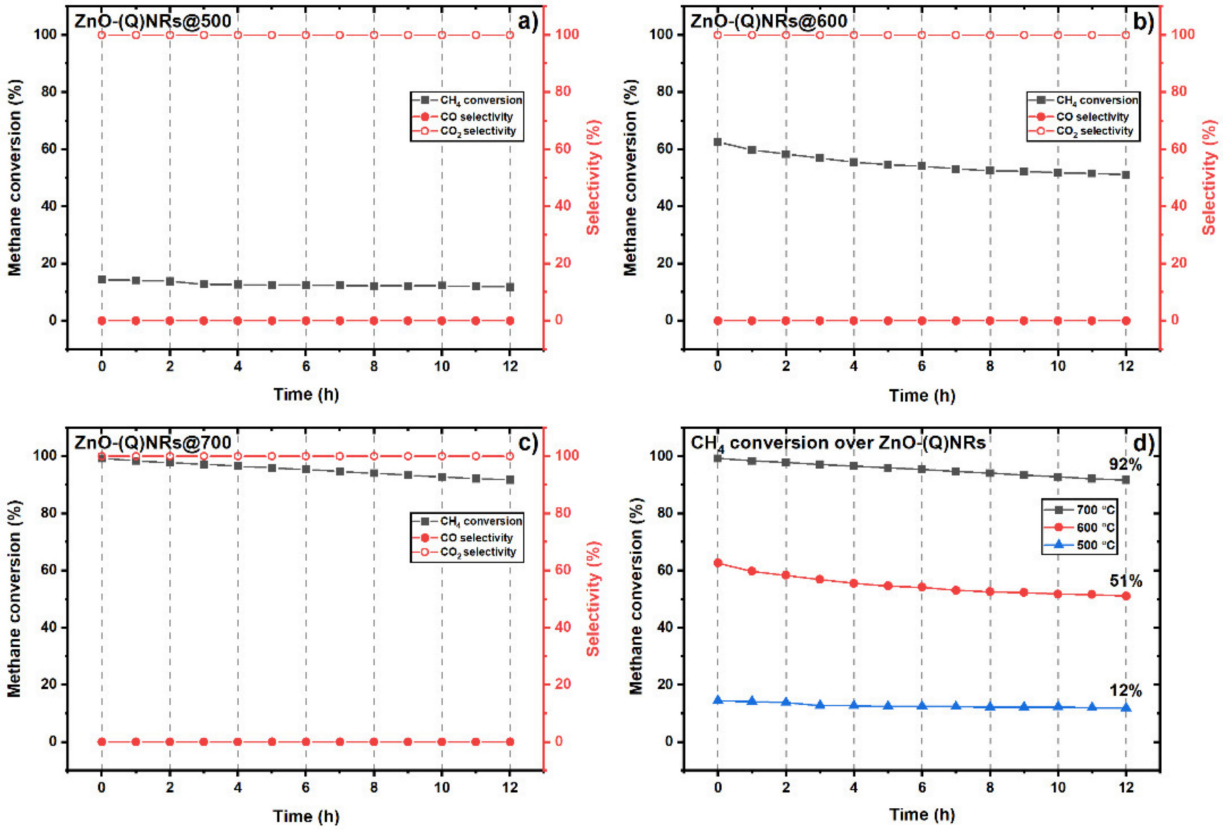

Figure 11. Time-on-stream (TOS) methane conversion (black) and CO and CO_2 selectivity (red) of methane combustion reactions catalyzed by ZnO-(Q)NRs at (**a**) 500 °C, (**b**) 600 °C, (**c**) 700 °C, and (**d**) a comparison of methane conversion at the three temperatures with the conversion values observed after 12 h shown as labels.

Based on the observed catalytic performances, the intrinsic activity and apparent activation energies (E_a) of the main ZnO-based catalysts were determined. Given the significantly different surface areas of the ZnO-nanomaterials in this study, the apparent reaction rates of methane combustion were normalized by the surface area to obtain surface-normalized reaction rates (r_{app}) in order to evaluate the intrinsic catalytic activity of the materials [88]. The r_{app} versus reaction temperature plot (Figure 12a) shows that the intrinsic catalytic activity followed the order ZnO-(Py)NRs > ZnO-NPys > ZnO-(Q)NRs, indicating that, despite a lower surface area, the first two materials displayed a higher density of active sites (oxygen vacancies or reducible oxygen species) than ZnO-(Q)NRs. Indeed, for ZnO-(Py)NRs, the higher intrinsic activity than ZnO-(Q)NRs and ZnO-NPys is justified by the higher abundance of oxygen vacancies based on O_2-TPD, PL, and XPS investigation (Figures 5–7). For ZnO-NPys, while displaying an identical proportion of oxygen vacancies to ZnO-(Q)NRs (Table 3), the H_2-TPR study in Figure 4 shows the presence of a larger amount of active oxygen species and a higher lattice oxygen mobility compared to ZnO-(Q)NRs based on the significantly higher hydrogen consumption and the lower reduction temperature. While both factors (reducibility and number of oxygen vacancies) are crucial for enhancing the catalytic performance in methane combustion [49], the larger amount of oxygen vacancies in ZnO-(Py)NRs seems to have a stronger effect than the higher reducibility of ZnO-NPys, resulting in a higher intrinsic activity for the former.

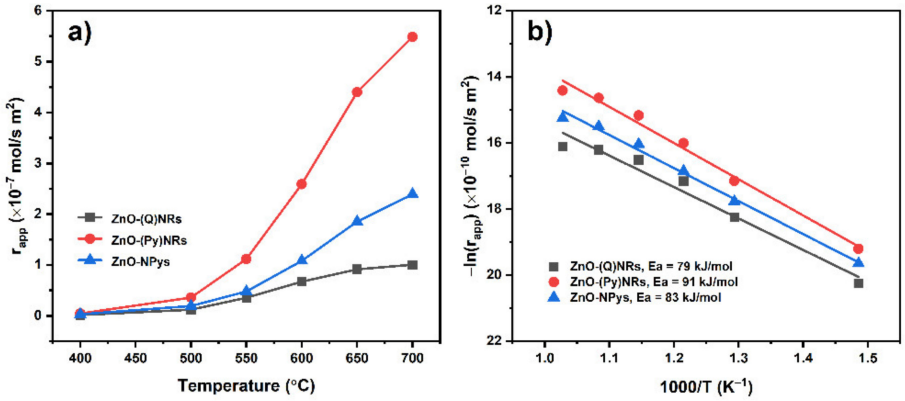

Figure 12. (**a**) Surface area-normalized apparent reaction rates (r_{app}) for ZnO-nanomaterials determined at various temperatures and (**b**) Arrhenius plot based on r_{app} values showing the calculated activation energies (E_a) of ZnO-based catalysts.

The apparent activation energy (E_a, Figure 12b) was evaluated by plotting ln(r_{app}) versus the reciprocal temperature 1000/T (K^{-1}) and by calculating the angular coefficient, E_a. Among the three catalysts, ZnO-(Q)NRs featured the lowest E_a value (79 kJ/mol) followed by ZnO-NPys (E_a = 83 kJ/mol) and ZnO-(Py)NRs (E_a = 91 kJ/mol). Nevertheless, the differences between the different materials were small, and all Ea values were found within the 85 ± 6 kJ/mol range. This observation indicates that all catalysts promoted the combustion of methane by a similar mechanism (i.e., by formation of active oxygen species at oxygen vacancies) and the main difference between the catalysts was likely to be found in the number of active sites due to the different surface area available for reaction. Such an effect was earlier observed also by Pecchi et al. in the $LaFeO_3$-catalyzed combustion of methane [117].

A comparative overview of the catalytic performance of ZnO-(Q)NRs with a selection of literature-reported catalysts such as perovskites, mixed metal oxides, and single-metal oxides is given in Table 5. Because variations of space velocity lead to significant changes in methane conversions [115], generally, only catalysts applied under similar conditions to ZnO-(Q)NRs (GHSV: 25,000–40,000) are considered. Comparison of the T_{50} and T_{90} temperatures for ZnO-(Q)NRs and perovskite-based catalysts (Table 5, entries 1–7) shows that the zinc-based system is a competitive alternative to the use of perovskites based on metals such as lanthanum, cobalt, and manganese.

Table 5. Comparison of catalytic performances between ZnO-(Q)NRs and literature-reported catalysts.

Entry	Catalyst	[CH_4] (vol%)	GHSV ($mL \cdot g_{cat}^{-1} \cdot h^{-1}$)	T_{50} (°C)	T_{90} (°C)	Ref.
1	$La_{0.7}Sr_{0.3}FeO_3$	4.35	26,700	580	-	[87]
2	$La_{0.6}Sr_{0.4}MnO_3$	2	30,000	566	661	[118]
3	$ZnO/La_{0.8}Sr_{0.2}CoO_3$	1	40,000	568	~650	[82]
4	3DOM [a] $La_{0.6}Sr_{0.4}MnO_3$	2	30,000	566	661	[119]
5	$La_{0.7}Ce_{0.3}CoO_3$	2	30,000	564	662	[45]
6	$CaMn_{0.6}Ti_{0.4}O_3$	3	30,000	585	-	[120]
7	ZnO-(Q)NRs	1	30,000	576	659	This work
8	CeO_2 [b]	1	30,000	632	-	[121]
9	α-Fe_2O_3 nanotubes	2	25,500	610	750	[122]
10	ZrO_2 nanobelts	2	25,000	650	700	[123]
11	3D-hm $La_{0.6}Sr_{0.4}MnO_3$ [c]	5	51,360	360	438	[69]
12	$Co_{0.95}Zr_{0.05}Cr_2O_4$	0.2	36,000	376	448	[124]
13	Co/Mn oxide (5:1) [d]	1	36,000	293	324	[72]

[a] 3DOM: three-dimensionally ordered macroporous structure. [b] Sample with 15.7 $m^2 \cdot g^{-1}$. [c] Disassembled mesostructured $La_{0.6}Sr_{0.4}MnO_3$ perovskite. [d] Mixed cobalt-manganese oxide prepared by coprecipitation.

Moreover, ZnO-(Q)NRs compare very well to other single-metal oxides of ceria, iron, and zirconia (Table 5, entries 7–10). Finally, the catalytic performance of ZnO-(Q)NRs and all catalysts in entries 1–10 in general is significantly lower than that reported for highly active materials such as 3D-hm $La_{0.6}Sr_{0.4}MnO_3$ (Table 5, entry 11) and cobalt-based mixed-metal oxides (Table 5, entries 12–13). Nevertheless, it is worth noting that the preparation of 3D-hm $La_{0.6}Sr_{0.4}MnO_3$ requires templating by large amounts of poly(methyl methacrylate), which might not be feasible on a large scale while the much higher cost of cobalt compared to zinc should also be taken into account. Additionally, according to a survey of catalytic performances in methane combustions [58], ZnO-(Q)NRs compare well to hexaaluminate catalysts, for which T_{90} values well above 700 °C are often encountered.

3. PL and XPS Investigation of Spent ZnO-(Q)NRs

To gain a deeper understanding of the good stability of the catalytic performance of ZnO-(Q)NRs in the TOS experiment despite aggregation, the PL spectrum of ZnO-(Q)NRs, retrieved after the TOS reaction at 700 °C, was investigated to explore potential modifications in the number and type of defect sites. Comparison of the PL spectra in Figure 13a (as-synthesized ZnO-(Q)NRs) and Figure 13b (ZnO-(Q)NRs after TOS reaction at 700 °C) shows an increase in intensity of the peak at 2.02 eV relative to double-charged oxygen vacancies compared to that attributed to O_{ads} centered at 1.71 eV for used ZnO-(Q)NRs and at 1.74 eV for pristine ZnO-(Q)NRs. Despite a strong decrease in surface area compared to the fresh catalyst, the increase in the relative amount of oxygen vacancies in the used ZnO-(Q)NRs may be beneficial to catalytic activity by offering more active sides for the activation of oxygen. Further investigation of this aspect was carried out by XPS spectroscopy (See below).

XPS spectroscopy (Figure 14) was employed to investigate changes in the O 1s components of the spent ZnO-(Q)NRs catalysts (after light-off investigation and after TOS reaction in the 500–700 °C temperature range) compared to the pristine materials (Figure 7a). In all cases, the O 1s region could be deconvoluted using the same three components O_I-O_{III} as the pristine material but with an observed increase in the O_{II} and O_{III} peaks intensities to the detriment of O_I, indicating an increased number of defects in the lattice and of adsorbed oxygen species. No significant binding energy change was observed for these components (Table S1) or for the position of the Zn 2p peaks of all materials shown in Figure 14. The variation of the relative intensities of the O 1s components after use of the ZnO-(Q)NRs under different conditions and temperatures is graphically shown in Figure 15. In all cases, under reaction conditions, the relative intensity of the O_I component decreased strongly along with a remarkable increase in the O_{II} and/or O_{III} components relative to oxygen vacancies and $O_{ads,}$ respectively. Focusing on the TOS reaction at 700 °C, by extending the reaction time from 12 h to 48 h (See Figure S16a,b for the XPS spectrum of the sample retrieved after 48 h), a further slight decrease in the O_I component with an increase in O_{II} was observed, indicating the progressive formation of oxygen vacancies under reaction conditions. Importantly, the formation of additional vacancies was not observed by simple calcination of ZnO-(Q)NRs in air under the same conditions as the TOS reaction (700 °C for 12 h, See Figure S16c,d for the XPS spectrum of calcined ZnO-(Q)NRs) indicating that the reaction with methane was responsible for the consumption of lattice oxygen and the increased formation of vacancies. Such vacancies, were, in turn, able to activate more oxygen from the feed, leading to an increase in O_{ads}. It is possible that the increased formation of oxygen vacancies and O_{ads} played a role in balancing the strong decrease in the surface area observed for ZnO-(Q)NRs at 700 °C, thus justifying the only slight drop of catalytic performance observed in Figure 11c after 12 h TOS.

Finally, it should be noted that investigation by Raman spectroscopy (Figure S17) of the as-prepared ZnO-(Q)NRs and those recovered after TOS reactions at 600 and 700 °C did not reveal the presence of the typical graphitic carbon-related D and G bands in the 1200–1800 cm^{-1} region, which are expected to form in the case of methane decomposition

and coking of the catalyst surface [125,126], thus excluding the occurrence of the latter reaction pathway.

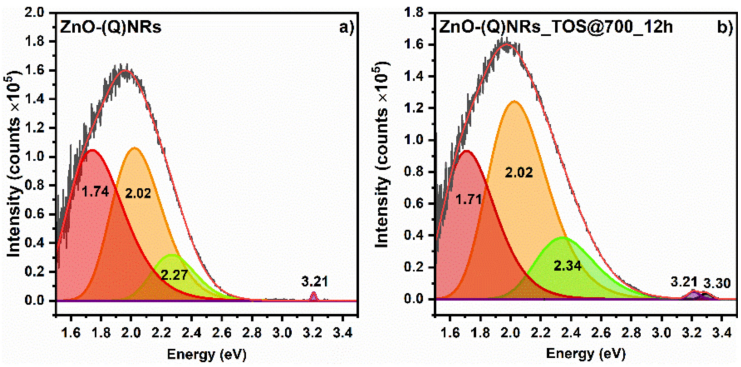

Figure 13. Photoluminescence spectra of as-synthesized ZnO-(Q)NRs (**a**) and after time on stream reaction at 700 °C (**b**). Excitation wavelength: 300 nm.

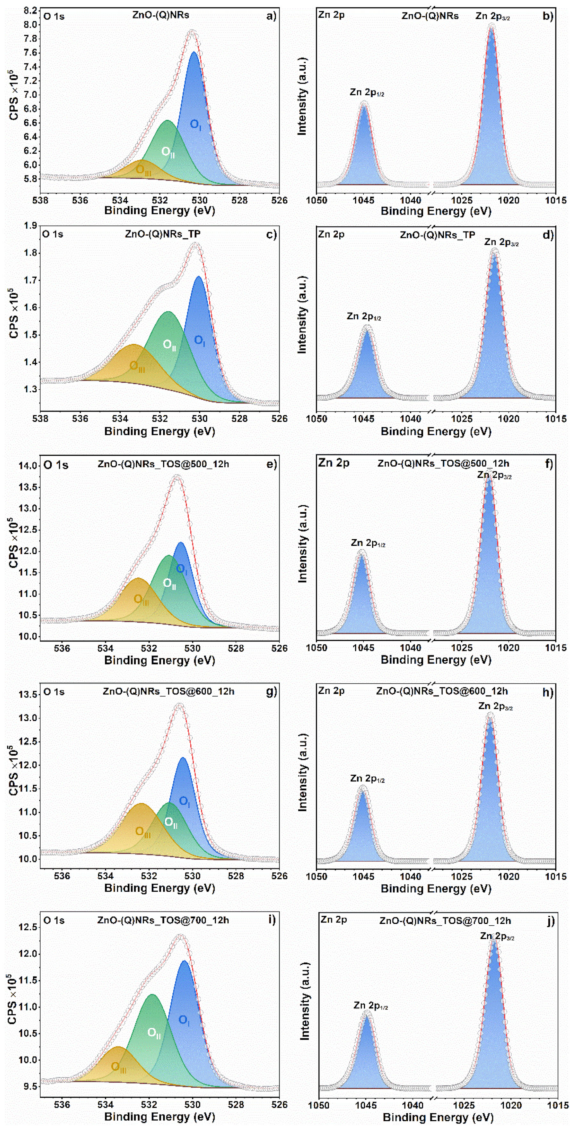

Figure 14. High-resolution XPS spectra of ZnO-(Q)NRs in the O 1s and background-subtracted Zn 2p spectral regions for pristine ZnO-(Q)NRs (**a**,**b**) temperature program (TP, light-off reaction) (**c**,**d**) and time-on-stream (TOS) reactions at (**e**,**f**) 500 °C, (**g**,**h**) 600 °C, and (**i**,**j**) 700 °C.

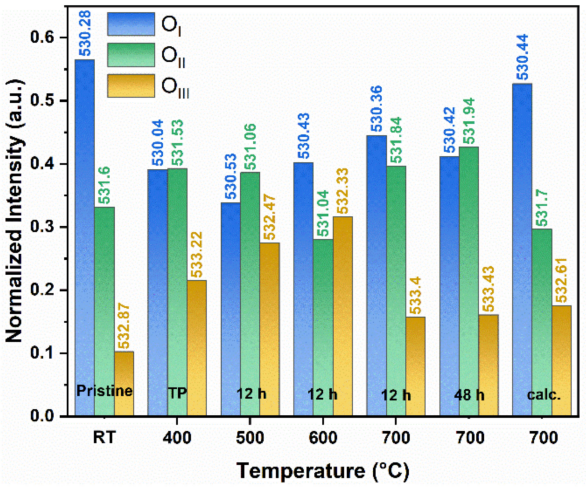

Figure 15. Relative intensities and binding energy values of XPS O 1s components of ZnO-(Q)NRs as-synthesized, after light-off curve investigation with temperature program (TP), after TOS reactions (500–700 °C, 12 h), and after TOS reaction at 700 °C, for 48 h and after calcination at 700 °C (12 h) in air.

4. Materials and Methods

4.1. Materials

Commercial zinc oxide was purchased from Daejung (ZnO-C). Anhydrous zinc acetate ($Zn(CH_3COO)_2$), zinc nitrate hexahydrate (98%) ($Zn(NO_3)_2{\cdot}6H_2O$), aluminum nitrate nonahydrate (98%) ($Al(NO_3)_3{\cdot}6H_2O$) was obtained from Alfa Aesar, Lancashire, UK. Benzyl amine (For synthesis) was purchased from Merck, dibenzyl ether (99%) was purchased from Acros Organics, Geel, Belgium, and hexamethylenetetramine (>99%) (HMTA) was obtained from Tokyo Chemical Industry (TCI), Tokyo, Japan. Diethyl ether (HPLC grade) was purchased from RCI Labscan Limited, Bangkok, Thailand. Absolute ethanol (99%) was obtained from Honeywell, Charlotte, NC, USA. Silicon dioxide (purum, >95%) (SiO_2) and lithium hydroxide (≥98%) (LiOH) were purchased from Sigma Aldrich, St. Louis, MO, USA.

4.2. Catalysts Preparation

4.2.1. Synthesis of ZnO Quantum Dots (ZnO-QDs)

The preparation of ZnO-QDs was based on the procedure developed by Daumann et al. [127], yet upscaled by four times. Briefly, $LiOH{\cdot}H_2O$ (16 mmol) was dissolved in 160 mL of absolute ethanol in a 250 mL 2-neck Schlenk flask under ultrasonication for 1 h. Following complete dissolution of $LiOH{\cdot}H_2O$, the solution was stirred and refluxed at 80 °C for 30 min under a nitrogen atmosphere. Anhydrous $Zn(CH_3COO)_2$ (16 mmol) was rapidly added to the solution. The mixture was further held at 80 °C for 5 min under continuous stirring and subsequently quenched in an ice bath. The mixture of dispersed ZnO nanoparticles was precipitated with hexane and centrifuged to obtain the ZnO-QDs. The ZnO-QDs were redispersed in ethanol and reprecipitated with hexane repeating the procedure two times. Finally, the ZnO-QDs were dried under a vacuum.

4.2.2. Synthesis of ZnO Nanopyramids (ZnO-NPys)

ZnO-NPy seeds were synthesized by the non-hydrolytic sol-gel method derived from Ahmad et al. [128] and readapted by Del Gobbo et al. [15,22]. Briefly, anhydrous $Zn(CH_3COO)_2$ (10 mmol, 1.8348 g) was loaded into a glass pressure vessel along with benzyl amine (10 mmol, 11 mL) and 30 mL of dibenzyl ether dried over molecular sieves. The mixture was then heated at 120 °C for 1 h to fully dissolve $Zn(CH_3COO)_2$. After dissolution, the temperature was increased up to 190 °C and kept constant for 24 h. All the steps were carried out under a nitrogen atmosphere. The synthesized ZnO-NPy seeds were then vacuum filtered using a PVDF membrane filter (0.22 µm pore size). The sample

was washed with absolute ethanol three times and a final time with diethyl ether. Finally, the obtained ZnO-NPys were dried under a vacuum overnight.

4.2.3. Synthesis of ZnO Nanorods

Synthesis of ZnO Nanorods from ZnO-QDs (ZnO-(Q)NRs)

The *s*ynthesis of ZnO-(Q)NRs was carried out as in previous reports [15,22], although slightly modified. A total of 200 mg of ZnO-QDs seeds were added to 500 mL of 50 mM $Zn(NO_3)_2 \cdot 6H_2O$ aqueous solution in 1 L Erlenmeyer flask. The mixture was sonicated for 1 h to completely disperse the ZnO-QDs. After that, 500 mL of 50 mM HMTA aqueous solution was added to the mixture. The mixture was heated up to 90 °C and kept at this temperature for *x* h (*x* = 1, 2, 6, 12). The formation of ZnO-(Q)NRs could be observed by the progressively increasing cloudiness of the mixture. The mixture was then cooled down in an ice bath. The white precipitates were obtained by vacuum filtration with a nitrocellulose membrane filter (0.45 µm pore size) and washed with large quantities of DI water. Finally, the ZnO-(Q)NRs were dried at 80 °C for 6 h.

Synthesis of ZnO Nanorods from ZnO-NPys (ZnO-(Py)NRs)

The synthesis of ZnO-(Py)NRs was carried out as in previous reports [15,22]. Briefly, the as-synthesized ZnO-NPy seeds (200 mg) were first added to a $Zn(NO_3)_2 \cdot 6H_2O$ (500 mL, 50 mM) solution. The mixture was then ultrasonicated for 1 h to well disperse the seeds. An HMTA (500 mL, 50 mM) solution was later added to the dispersed zinc mix, resulting in a $Zn(NO_3)_2 \cdot 6H_2O$ and HTMA 25 mM solution. The combined solution was then heated at 90 °C for *x* h (*x* = 1, 12). Afterward, the mixture was quenched in an ice bath, then vacuum filtered with a nitrocellulose membrane (0.45 µm pore size). The sample was abundantly washed with deionized water before freeze-drying overnight to obtain ZnO-(Py)NRs.

4.3. Catalyst Characterizations

4.3.1. Scanning Electron Microscopy (SEM)

Morphological images of ZnO-based catalysts were acquired by a JEOL JSM-7610F field emission scanning electron microscope, Peabody, MA, USA, equipped with an Oxford Instruments X-Max150 EDS, Oxfordshire, UK. Samples were prepared by lightly tapping carbon adhesive tape attached to a sample stub onto paper smeared with ZnO powder. All samples were metalized with Pd before the measurements.

4.3.2. Powder X-ray Diffraction (PXRD)

PXRD patterns were acquired on annealed ZnO-NRs powder by using a Bruker Discovery D8 diffractometer, Billerica, MA, USA, in powder configuration using the rotating sample with anti-air scatter options without an entrance slit. The interplanar distance (d) was calculated by using Bragg's equation for the determination: $n\lambda = 2d \sin\theta$, where θ is the angle between normal to diffracting plane and incident X-ray, λ is the wavelength of X-rays, ($\lambda_{Cu\ K\alpha} = 1.5405$ Å). The a and c lattice constants were calculated using the following expression for hexagonal lattice where h, k, and l are the Miller indexes (Equation (1)).

$$\frac{1}{d^2} = \frac{4}{3}\left(\frac{h^2 + hk + l^2}{a^2}\right) + \frac{l^2}{c^2} \quad (1)$$

The main peaks' 2θ values were obtained by fitting the diffraction peaks by a pseudo-Voigt line shape.

4.3.3. X-ray Photoelectron Spectroscopy (XPS)

X-ray photoelectron spectroscopy (XPS) was performed on a JEOL JPS-9010MC spectrometer, Peabody, MA, USA, utilizing a Mg Kα source (1253.6 eV) working at 12 kV and 25 mA. All XPS spectra were acquired under high vacuum (10^{-8} Pa) at room temperature. A dried carbon tape support was coated with the ZnO samples. The survey scans were

acquired with a pass energy of 50 eV, a binding energy range of 0–1100 eV, and steps of 1 eV. Deconvolution of the high-resolution spectra was carried out using CasaXPS software, Teignmouth, UK, applying Shirley-type background along with symmetric and asymmetric convoluted Gaussian-Lorentzian line shapes (LA and LF). All spectral energies were referenced to the adventitious carbon peak C 1s B.E. = 284.80 eV.

4.3.4. Photoluminescence Measurements (PL)

Steady-state photoluminescence measurements were carried out on an Edinburgh Instruments FLS 980 spectrometer, Livingston, UK, equipped with a monochromatized Xe lamp as the excitation light source and photomultiplier near UV-visible range detector. The samples were loaded in powder form in a quartz solid cuvette oriented at 45° to minimize the 0° reflected exciting radiation entering the detector. The excitation wavelength used was 300 nm.

4.3.5. BET Surface Area Determination

The Brunauer–Emmett–Teller (BET) surface areas were determined by the nitrogen adsorption-desorption measurements obtained at liquid N_2 temperature (−196 °C) using the BELSORP-miniII, Osaka, Japan. Prior to the measurements, each sample (50–70 mg) was pretreated at 300 °C for 12 h under a vacuum. The specific surface areas were calculated using BELMaster software, Osaka, Japan.

4.3.6. H_2-Temperature Programmed Reduction (H_2-TPR)

H_2-TPR of different catalysts were attained on a BELCATII catalyst analyzer with a thermal conductivity detector (TCD) from MicrotracBEL Corp, Osaka, Japan. The sample was pretreated in flowing argon (50 sccm) at 300 °C for 120 min with a heating rate of 10 °C/min and later cooled down to 40 °C. Next, flowing Ar was switched to 2% H_2/Ar for 60 min to ensure detector stability. TPR measurements under 2% H_2/Ar (50 sccm) started at 40 °C to 800 °C with a heating rate of 10 °C/min and maintained at 800 °C for 60 min.

4.3.7. O_2-Temperature Programmed Desorption (O_2-TPD)

O_2-TPD of different catalysts were attained on a BELCATII catalyst analyzer with a thermal conductivity detector (TCD) from MicrotracBEL Corp., Osaka, Japan. The samples were pretreated in flowing helium (50 sccm) at 550 °C for 30 min and at 500 °C for 60 min with a heating rate of 10 °C/min and later cooled down to 50 °C. Next, flowing He was switched to 5% O_2/He and maintained for 120 min to allow adsorption between O_2 molecules and the surface of the samples. The gas was then switched back to He for another 60 min to remove any loosely adsorbed O_2 molecules and ensure detector stability. TPD measurements under He (30 sccm) started at 50 °C to 700 °C with a heating rate of 10 °C/min and maintained at 700 °C for 60 min.

4.4. Catalytic Activity Tests

4.4.1. Catalytic Activity Test Setup

The catalytic activity measurements were performed in an assembled system constituted by a computer-controlled three mass-flow controllers Bronkhorst EL-FLOW *Select*, Ruurlo, The Netherlands, calibrated for CH_4, N_2, and air zero connected to the reactor through a manifold (Scheme 1). The U-shaped tube quartz reactor (ID 7 mm) was placed in a temperature-programmed vertical tubular Carbolite Gero furnace, Derbyshire, UK, capable of a maximum operating temperature of 1200 °C. The outlet of the reactor was connected to a gas chromatography system (Perkin Elmer Clarus® 580 GC system, Waltham, MA, USA) mounting a total of four packed columns for gas separation i.e., 7′ HayeSep N 1/8″ Sf, 9′ Molecular Sieve 13X 1/8″ Sf, 9′ Molecular Sieve 5A, 1/8″ Sf, and 4′ HayeSep T, 1/8″ Sf, coupled with TCD detectors, which were used to analyze the gaseous reaction products qualitatively and quantitatively.

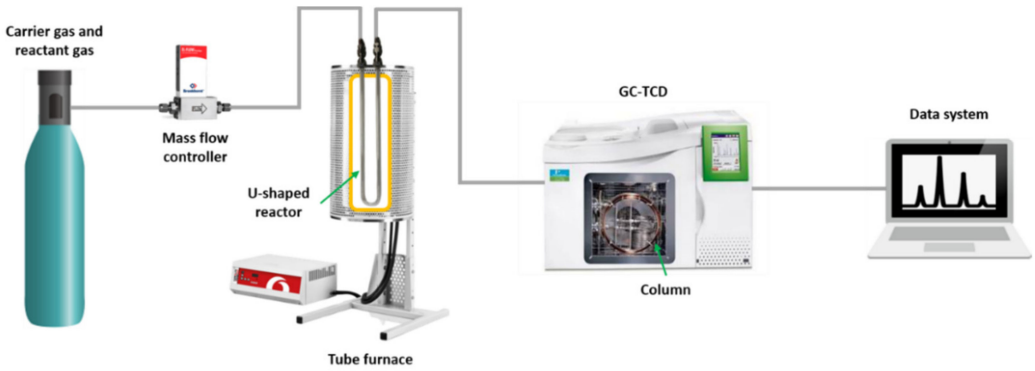

Scheme 1. Custom-assembled catalytic test setup.

4.4.2. Light-Off Curve Determination with Temperature Program

For every catalytic test, the ZnO-based catalyst (200 mg) was diluted with quartz silica, homogenized by soft mixing in a mortar and loaded in the quartz tube, filling the bottom end of the U-shaped quartz reactor section. The powder was blocked at the extremities with quartz wool to prevent the flush of the silica/catalyst mixture. Prior to the catalysis test, the catalysts were exposed to N_2 (20 mL/min) at room temperature for 2 h, and subsequently during heat ramping to 400 °C to remove possible impurities, in particular, moisture. The catalytic test was carried out by continuously flowing the reactant gases, comprised of 1% CH_4 and 99% Air zero (20.79% O_2, 78.21% N_2) through the catalyst bed at a total flow rate of 100 mL/min. To stabilize the gas flow, the reactant gases were passed through the system at 400 °C for one hour prior to the actual test. The tests were performed from 400 °C to 700 °C with 50 °C increment intervals and with a heating rate of 5 °C/min. For each temperature, two 12 min GC acquisitions were carried out and the quantification results were averaged.

4.4.3. Time on Stream Test (TOS)

The catalyst was loaded in the reactor as described above. Before each test, the catalysts were exposed to N_2 (20 mL/min) at room temperature for 2 h, and subsequently during the heating process up to the set point temperature (i.e., 500, 600, and 700 °C) with a heating rate of 5 °C/min to remove moisture. A mixture of 1% CH_4 and 99% Air zero reactant gases were led continuously over the catalyst bed at a total flow rate of 100 mL/min. For flow stabilization, the reactant gases were flowed through the system at the set point temperature for one hour prior to the test. The measurement was monitored every hour by GC-TCD for a total of 12 h.

The CH_4 conversion and CO and CO_2 selectivity was determined by the quantity of carbon-based products relative to the initial carbon-based content (Equations (2)–(4)). [CO], [CO_2], and [CH_4] are the concentrations of outlet gases obtained by integrating the peaks of the chromatogram [129,130].

$$CH_4 \text{ converison } (\%) = \frac{[CO] + [CO_2]}{[CO] + [CO_2] + [CH_4]} \times 100 \quad (2)$$

$$CO \text{ selectivity } (\%) = \frac{CO}{(CO + CO_2)} \times 100 \quad (3)$$

$$CO_2 \text{ selectivity } (\%) = \frac{CO_2}{(CO + CO_2)} \times 100 \quad (4)$$

5. Conclusions

The combustion of methane is a crucially important process in the field of energy generation and oil extraction, but it leads to the emissions of noxious gases The catalytic combustion of methane can alleviate the environmental issues related to the combustion

of methane in flame, and its widespread implementation is likely to require inexpensive and highly available metal oxides. Catalysts able to operate in the 600–800 °C temperature range can lead to a significant drop in toxic emissions. Compared to increasingly expensive metals such as cobalt and nickel and to increasingly exploited metals such as lanthanum and manganese, whose availability is geographically restricted, zinc is abundant, inexpensive, and ubiquitously available. Therefore, in this work, quasi-1D ZnO-nanostructures were successfully used for the catalytic selective combustion of methane. Among such nanomaterials, ZnO-(Q)NRs, prepared in just one hour from ZnO quantum dots, showed a relatively high surface area and provided the most efficient methane combustion in terms of T_{50} (576 °C) and T_{90} (659 °C) values. Importantly such temperature values compared well with those reported for numerous perovskite-based catalysts, hexaaluminates, and other single-metal oxides. Spectroscopic investigation of the ZnO-nanomaterials used in this work showed the presence of abundant oxygen vacancies and defect sites when compared to commercial zinc oxide (ZnO-C). Whereas materials such as ZnO-(Py)NRs and ZnO-NPys showed a higher density of active sites than ZnO-(Q)NRs, and therefore a higher intrinsic catalytic activity, the larger surface area of the latter ensured a better catalytic performance. These results suggest that the future design of ZnO-nanomaterials combining high surface area and abundant vacant sites will be crucial to obtain even more efficient catalytic performances. Time-on-stream investigation using ZnO-(Q)NRs showed that complete conversion of methane could be obtained at 700 °C and that the methane conversion remained over 90% after 12 h despite the strong sintering of nanorods. Through a systematic post-reaction characterization, the latter result was attributed to the formation of abundant oxygen vacancies on the surface of ZnO-(Q)NRs by treatment at 700 °C, likely enhancing its catalytic performance and compensating the loss of surface area.

Overall, the results in this paper show that ZnO-nanomaterials with high surface areas have the potential to serve as readily available catalysts for the combustion of methane in the 600–700 °C temperature range and are therefore suitable inexpensive materials for some important applications such as combustion of residual methane from gas turbines.

Supplementary Materials: The following supporting information can be downloaded at: https://www.mdpi.com/article/10.3390/catal12121533/s1, Figure S1. SEM images of ZnO-NPys, Figure S2. (**a**) TEM image of pristine ZnO-QDs used as seeds for the growth of ZnO-(Q)NRs and (**b**) their size distribution (diameter) reported as a histogram and overlying Gaussian distribution, Figure S3. Statistical distribution of diameter and length represented by histograms with overlying Gaussian distributions of ZnO-(Q)NRs synthesized in (**a**,**b**) 1h, (**c**,**d**) 2h, (**e**,**f**) 6h, and (**g**,**h**) 12h, Figure S4. Size distribution histograms with overlying Gaussian distributions of ZnO-(Py)NRs synthesized in (**a**,**b**) 1 h and (**c**,**d**) 12 h, respectively, Figure S5. Adsorption isotherms of ZnO-(Q)NRs synthesized in (**a**) 1, (**b**) 2, (**c**) 6, and (**d**) 12 h, Figure S6. Adsorption isotherms of ZnO-(Py)NRs synthesized in (**a**) 1 and (**b**) 12 h, (**c**) ZnO-NPys, and (**d**) ZnO-C, Table S1. O1s and Zn2p XPS peak positions obtained from deconvolution, Figure S7. SEM images of commercial ZnO (ZnO-C), Figure S8. SEM images of ZnO-(Py)NRs, Figure S9. XRD patterns of ZnO-(Py)NRs, Figure S10: XRD patterns of ZnO-NPys, Figure S11. XRD patterns of the pristine ZnO-C and after use in the 400 °C to 700 °C temperature range, Table S2. Physical properties of ZnO catalysts, Figure S12. The trend of methane conversion and CO2 selectivity versus reaction temperature (light-off curves), Figure S13. Comparison of methane conversion of silica dilutant (SiO2), ZnO-C and synthesized ZnO catalysts under the temperature program (TP) from 400 °C to 700 °C, Figure S14. Time-on-stream (TOS) methane conversion (black) and CO and CO_2 selectivity (red) of methane combustion reactions catalyzed by ZnO-(Py)NRs, Figure S15. Time-on-stream (TOS) methane conversion (black) and CO and CO_2 selectivity (red) of methane combustion reactions catalyzed by ZnO-NPys, Figure S16. High-resolution XPS spectra of ZnO-(Q)NRs in the O 1s and background-subtracted Zn 2p spectral regions, Figure S17. Standard Normal Variate (SNV) normalized Raman intensity of the as-prepared ZnO-(Q)NRs, ZnO-(Q)NRs retrieved after the TOS experiment at 600 °C for 12h, and ZnO-(Q)NRs retrieved after the TOS experiment at 700 °C for 12h.

Author Contributions: Conceptualization, V.D. and S.D.G.; methodology, T.K. and S.S., validation, T.S., V.D. and S.D.G.; investigation, T.K., S.S. and S.D.G.; resources, V.D.; data curation, V.D.; writing—original draft preparation, T.K. and S.D.G.; writing—review and editing, T.S. and V.D.; visualization, S.D.G.; supervision, V.D. and T.S.; funding acquisition, V.D. All authors have read and agreed to the published version of the manuscript.

Funding: V.D. acknowledges the National Research Council of Thailand (grants N41A640170 and N42A650196) for funding this research. S.D.G acknowledges financial support through a postdoctoral fellowship from the Vidyasirimedhi Institute of Science and Technology (VISTEC).

Data Availability Statement: All data are generally available in the manuscript and Supporting Information. Additional data are available upon request from the corresponding author.

Conflicts of Interest: The authors declare no conflict of interest.

References

1. Sun, Y.; Chen, L.; Bao, Y.; Zhang, Y.; Wang, J.; Fu, M.; Wu, J.; Ye, D. The Applications of Morphology Controlled ZnO in Catalysis. *Catalysts* **2016**, *6*, 188. [CrossRef]
2. Ong, C.B.; Ng, L.Y.; Mohammad, A.W. A review of ZnO nanoparticles as solar photocatalysts: Synthesis, mechanisms and applications. *Renew. Sustain. Energy Rev.* **2018**, *81*, 536–551. [CrossRef]
3. Hamid, S.B.A.; Teh, S.J.; Lai, C.W. Photocatalytic Water Oxidation on ZnO: A Review. *Catalysts* **2017**, *7*, 93. [CrossRef]
4. Goktas, S.; Goktas, A. A comparative study on recent progress in efficient ZnO based nanocomposite and heterojunction photocatalysts: A review. *J. Alloys Compd.* **2021**, *863*, 158734. [CrossRef]
5. Pandey, R.K.; Dutta, J.; Brahma, S.; Rao, B.; Liu, C.-P. Review on ZnO-based piezotronics and piezoelectric nanogenerators: Aspects of piezopotential and screening effect. *J. Phys. Mater.* **2021**, *4*, 44011. [CrossRef]
6. Puspasari, V.; Ridhova, A.; Hermawan, A.; Amal, M.I.; Khan, M.M. ZnO-based antimicrobial coatings for biomedical applications. *Bioprocess Biosyst. Eng.* **2022**, *45*, 1421–1445. [CrossRef]
7. Kang, Y.; Yu, F.; Zhang, L.; Wang, W.; Chen, L.; Li, Y. Review of ZnO-based nanomaterials in gas sensors. *Solid State Ion.* **2021**, *360*, 115544. [CrossRef]
8. Rahman, F. Zinc oxide light-emitting diodes: A review. *Opt. Eng.* **2019**, *58*, 10901. [CrossRef]
9. Lee, Y.H.; Ha, M.; Song, I.; Lee, J.H.; Won, Y.; Lim, S.; Ko, H.; Oh, J.H. High-Performance Hybrid Photovoltaics with Efficient Interfacial Contacts between Vertically Aligned ZnO Nanowire Arrays and Organic Semiconductors. *ACS Omega* **2019**, *4*, 9996–10002. [CrossRef] [PubMed]
10. Wibowo, A.; Marsudi, M.A.; Amal, M.I.; Ananda, M.B.; Stephanie, R.; Ardy, H.; Diguna, L.J. ZnO nanostructured materials for emerging solar cell applications. *RSC Adv.* **2020**, *10*, 42838–42859. [CrossRef] [PubMed]
11. Ouyang, W.; Chen, J.; Shi, Z.; Fang, X. Self-powered UV photodetectors based on ZnO nanomaterials. *Appl. Phys. Rev.* **2021**, *8*, 31315. [CrossRef]
12. Chen, H.; Cui, H.; Lv, Y.; Liu, P.; Hao, F.; Xiong, W.; Luo, H.a. CO_2 hydrogenation to methanol over Cu/ZnO/ZrO2 catalysts: Effects of ZnO morphology and oxygen vacancy. *Fuel* **2022**, *314*, 123035. [CrossRef]
13. Li, D.; Xu, F.; Tang, X.; Dai, S.; Pu, T.; Liu, X.; Tian, P.; Xuan, F.; Xu, Z.; Wachs, I.E.; et al. Induced activation of the commercial Cu/ZnO/Al2O3 catalyst for the steam reforming of methanol. *Nat. Catal.* **2022**, *5*, 99–108. [CrossRef]
14. Yusuff, A.S.; Bhonsle, A.K.; Trivedi, J.; Bangwal, D.P.; Singh, L.P.; Atray, N. Synthesis and characterization of coal fly ash supported zinc oxide catalyst for biodiesel production using used cooking oil as feed. *Renew. Energy* **2021**, *170*, 302–314. [CrossRef]
15. Del Gobbo, S.; Poolwong, J.; D'Elia, V.; Ogawa, M. Simultaneous Controlled Seeded-Growth and Doping of ZnO Nanorods with Aluminum and Cerium: Feasibility Assessment and Effect on Photocatalytic Activity. *Cryst. Growth Des.* **2020**, *20*, 5508–5525. [CrossRef]
16. Sanakousar, F.M.; Vidyasagar, C.C.; Jiménez-Pérez, V.M.; Prakash, K. Recent progress on visible-light-driven metal and non-metal doped ZnO nanostructures for photocatalytic degradation of organic pollutants. *Mater. Sci. Semicond. Process.* **2022**, *140*, 106390. [CrossRef]
17. Sofianos, V.M.; Lee, J.; Silvester, D.S.; Samanta, P.K.; Paskevicius, M.; English, N.J.; Buckley, C.E. Diverse morphologies of zinc oxide nanoparticles and their electrocatalytic performance in hydrogen production. *J. Energy Chem.* **2021**, *56*, 162–170. [CrossRef]
18. Yu, D.; Jia, Y.; Yang, Z.; Zhang, H.; Zhao, J.; Zhao, Y.; Weng, B.; Dai, W.; Li, Z.; Wang, P.; et al. Solar Photocatalytic Oxidation of Methane to Methanol with Water over $RuO_x/ZnO/CeO_2$ Nanorods. *ACS Sustain. Chem. Eng.* **2021**, *10*, 16–22. [CrossRef]
19. Wolf, J.; Sandstead, H.H.; Rink, L. Zinc. In *Handbook on the Toxicology of Metals*; Volume II: Specific Metals; Academic Press: Cambridge, MA, USA, 2022; pp. 963–984.
20. Hessien, M. Recent progress in zinc oxide nanomaterials and nanocomposites: From synthesis to applications. *Ceram. Int.* **2022**, *48*, 22609–22628. [CrossRef]
21. Primc, G.; Brenčič, K.; Mozetič, M.; Gorjanc, M. Recent Advances in the Plasma-Assisted Synthesis of Zinc Oxide Nanoparticles. *Nanomaterials* **2021**, *11*, 1191. [CrossRef] [PubMed]

22. Del Gobbo, S.; Poolwong, J.; D'Elia, V. In-Suspension Growth of ZnO Nanorods with Tunable Length and Diameter Using Polymorphic Seeds. *Cryst. Growth Des.* **2019**, *19*, 6792–6800. [CrossRef]
23. Aspoukeh, P.K.; Barzinjy, A.A.; Hamad, S.M. Synthesis, properties and uses of ZnO nanorods: A mini review. *Int. Nano Lett.* **2021**, *12*, 153–168. [CrossRef]
24. Saputra, I.S.; Apriandanu, D.O.B.; Yulizar, Y.; Maryanti, E.; Permana, Y.N.; Suhartati, S.; Sudirman. A facile preparation of ZnO/Au nano-needles: Optical, morphological and structural properties. *Opt. Mater.* **2021**, *121*, 111628. [CrossRef]
25. Noh, Y.; Jeong, H.; Lee, D. Enhanced ultraviolet photodetector using zinc oxide nanowires with intense pulsed light post-treatment. *J. Alloys Compd.* **2021**, *871*, 159537. [CrossRef]
26. Ali, M.; Tit, N.; Yamani, Z.H. Role of defects and dopants in zinc oxide nanotubes for gas sensing and energy storage applications. *Int. J. Energy Res.* **2020**, *44*, 10926–10936. [CrossRef]
27. Naderi, S.; Javaheri, S.; Shahrokhi, M.; Nia, B.A.; Shahmoradi, S. Optical properties of zigzag and armchair ZnO nanoribbons. *Phys. E Low-Dimens. Syst. Nanostruct.* **2020**, *124*, 114218. [CrossRef]
28. Pan, X.; Zhao, X. Ultra-High Sensitivity Zinc Oxide Nanocombs for On-Chip Room Temperature Carbon Monoxide Sensing. *Sensors* **2015**, *15*, 8919–8930. [CrossRef]
29. Peng, Y.; Xu, A.-W.; Deng, B.; Antonietti, M.; Cölfen, H. Polymer-Controlled Crystallization of Zinc Oxide Hexagonal Nanorings and Disks. *J. Phys. Chem. B* **2006**, *110*, 2988–2993. [CrossRef] [PubMed]
30. Ha, L.P.P.; Vinh, T.H.T.; Thuy, N.T.B.; Thi, C.M.; Viet, P.V. Visible-light-driven photocatalysis of anisotropic silver nanoparticles decorated on ZnO nanorods: Synthesis and characterizations. *J. Environ. Chem. Eng.* **2021**, *9*, 105103. [CrossRef]
31. Moon, D.-B.; Bag, A.; Lee, H.-B.; Meeseepong, M.; Lee, D.-H.; Lee, N.-E. A stretchable, room-temperature operable, chemiresistive gas sensor using nanohybrids of reduced graphene oxide and zinc oxide nanorods. *Sens. Actuators B Chem.* **2021**, *345*, 130373. [CrossRef]
32. Patzke, G.R.; Krumeich, F.; Nesper, R. Oxidic Nanotubes and Nanorods—Anisotropic Modules for a Future Nanotechnology. *Angew. Chem. Int. Ed.* **2002**, *41*, 2446–2461. [CrossRef]
33. McLaren, A.; Valdes-Solis, T.; Li, G.; Tsang, S.C. Shape and Size Effects of ZnO Nanocrystals on Photocatalytic Activity. *J. Am. Chem. Soc.* **2009**, *131*, 12540–12541. [CrossRef] [PubMed]
34. Ma, C.; Jin, W.; Duan, X.; Ma, X.; Han, H.; Zhang, Z.; Yu, J.; Wu, Y. From the absolute surface energy to the stabilization mechanism of high index polar surface in wurtzite structure: The case of ZnO. *J. Alloys Compd.* **2019**, *772*, 482–488. [CrossRef]
35. Ayoub, I.; Kumar, V.; Abolhassani, R.; Sehgal, R.; Sharma, V.; Sehgal, R.; Swart, H.C.; Mishra, Y.K. Advances in ZnO: Manipulation of defects for enhancing their technological potentials. *Nanotechnol. Rev.* **2022**, *11*, 575–619. [CrossRef]
36. Bernard, P.; Stelmachowski, P.; Broś, P.; Makowski, W.; Kotarba, A. Demonstration of the Influence of Specific Surface Area on Reaction Rate in Heterogeneous Catalysis. *J. Chem. Educ.* **2021**, *98*, 935–940. [CrossRef] [PubMed]
37. Poolwong, J.; Del Gobbo, S.; D'Elia, V. Transesterification of dimethyl carbonate with glycerol by perovskite-based mixed metal oxide nanoparticles for the atom-efficient production of glycerol carbonate. *J. Ind. Eng. Chem.* **2021**, *104*, 43–60. [CrossRef]
38. Liu, X.; Chen, C. Mxene enhanced the photocatalytic activity of ZnO nanorods under visible light. *Mater. Lett.* **2020**, *261*, 127127. [CrossRef]
39. Chen, Z.; Fang, Y.; Wang, L.; Chen, X.; Lin, W.; Wang, X. Remarkable oxygen evolution by Co-doped ZnO nanorods and visible light. *Appl. Catal. B Environ.* **2021**, *296*, 120369. [CrossRef]
40. Wang, H.; Dai, M.; Li, Y.; Bai, J.; Liu, Y.; Li, Y.; Wang, C.; Liu, F.; Lu, G. The influence of different ZnO nanostructures on NO_2 sensing performance. *Sens. Actuators B Chem.* **2021**, *329*, 129145. [CrossRef]
41. Verma, S.; Tirumala Rao, B.; Singh, R.; Kaul, R. Photocatalytic degradation kinetics of cationic and anionic dyes using Au–ZnO nanorods: Role of pH for selective and simultaneous degradation of binary dye mixtures. *Ceram. Int.* **2021**, *47*, 34751–34764. [CrossRef]
42. Lim, S.K.; Hwang, S.-H.; Kim, S.; Park, H. Preparation of ZnO nanorods by microemulsion synthesis and their application as a CO gas sensor. *Sens. Actuators B Chem.* **2011**, *160*, 94–98. [CrossRef]
43. Chen, M.-H.; Lu, Q.-Y.; Li, Y.-M.; Chu, M.-M.; Cao, X.-B. ZnO@ZIF-8 core–shell heterostructures with improved photocatalytic activity. *CrystEngComm* **2021**, *23*, 4327–4335. [CrossRef]
44. Wang, Y.; Ren, J.; Wang, Y.; Zhang, F.; Liu, X.; Guo, Y.; Lu, G. Nanocasted Synthesis of Mesoporous LaCoO3 Perovskite with Extremely High Surface Area and Excellent Activity in Methane Combustion. *J. Phys. Chem. C* **2008**, *112*, 15293–15298. [CrossRef]
45. Arandiyan, H.; Scott, J.; Wang, Y.; Dai, H.; Sun, H.; Amal, R. Meso-Molding Three-Dimensional Macroporous Perovskites: A New Approach to Generate High-Performance Nanohybrid Catalysts. *ACS Appl. Mater. Interfaces* **2016**, *8*, 2457–2463. [CrossRef] [PubMed]
46. Kucharczyk, B.; Okal, J.; Tylus, W.; Winiarski, J.; Szczygieł, B. The effect of the calcination temperature of LaFeO3 precursors on the properties and catalytic activity of perovskite in methane oxidation. *Ceram. Int.* **2019**, *45*, 2779–2788. [CrossRef]
47. Fan, X.; Li, L.; Yang, X.; Guo, Z.; Jing, F.; Chu, W. High-performance $Co_xM_{3-x}AlO_y$ (M=Ni, Mn) catalysts derived from microwave-assisted synthesis of hydrotalcite precursors for methane catalytic combustion. *Catal. Today* **2020**, *347*, 23–30. [CrossRef]
48. Tao, F.F.; Shan, J.-j.; Nguyen, L.; Wang, Z.; Zhang, S.; Zhang, L.; Wu, Z.; Huang, W.; Zeng, S.; Hu, P. Understanding complete oxidation of methane on spinel oxides at a molecular level. *Nat. Commun.* **2015**, *6*, 7798. [CrossRef]

49. Yang, J.; Hu, S.; Shi, L.; Hoang, S.; Yang, W.; Fang, Y.; Liang, Z.; Pan, C.; Zhu, Y.; Li, L.; et al. Oxygen Vacancies and Lewis Acid Sites Synergistically Promoted Catalytic Methane Combustion over Perovskite Oxides. *Environ. Sci. Technol.* **2021**, *55*, 9243–9254. [CrossRef]
50. Campagnoli, E.; Tavares, A.C.; Fabbrini, L.; Rossetti, I.; Dubitsky, Y.A.; Zaopo, A.; Forni, L. $La_{1-x}A'_xCo_{1-y}Fe_yO_{3\pm\delta}$ (A′=Ce,Sr) catalysts for the flameless combustion of methane. *J. Mater. Sci.* **2006**, *41*, 4713–4719. [CrossRef]
51. Bashan, V.; Ust, Y. Perovskite catalysts for methane combustion: Applications, design, effects for reactivity and partial oxidation. *Int. J. Energy Res.* **2019**, *43*, 7755–7789. [CrossRef]
52. Chang-Ke, W.; Xin-Zheng, L.; Hua, Z. Shares Differences of Greenhouse Gas Emissions Calculated with GTP and GWP for Major Countries. *Adv. Clim. Change Res.* **2013**, *4*, 127–132. [CrossRef]
53. Bui, M.; Adjiman, C.S.; Bardow, A.; Anthony, E.J.; Boston, A.; Brown, S.; Fennell, P.S.; Fuss, S.; Galindo, A.; Hackett, L.A.; et al. Carbon capture and storage (CCS): The way forward. *Energy Environ. Sci.* **2018**, *11*, 1062–1176. [CrossRef]
54. D'Elia, V.; Kleij, A.W. Surface science approach to the heterogeneous cycloaddition of CO_2 to epoxides catalyzed by site-isolated metal complexes and single atoms: A review. *Green Chem. Eng.* **2022**, *3*, 210–227. [CrossRef]
55. Sodpiban, O.; Phungpanya, C.; Del Gobbo, S.; Arayachukiat, S.; Piromchart, T.; D'Elia, V. Rational engineering of single-component heterogeneous catalysts based on abundant metal centers for the mild conversion of pure and impure CO_2 to cyclic carbonates. *Chem. Eng. J.* **2021**, *422*, 129930. [CrossRef]
56. Xie, W.-H.; Li, H.; Yang, M.; He, L.-N.; Li, H.-R. CO_2 capture and utilization with solid waste. *Green Chem. Eng.* **2022**, *3*, 199–209. [CrossRef]
57. He, L.; Fan, Y.; Bellettre, J.; Yue, J.; Luo, L. A review on catalytic methane combustion at low temperatures: Catalysts, mechanisms, reaction conditions and reactor designs. *Renew. Sustain. Energy Rev.* **2020**, *119*, 109589. [CrossRef]
58. Tian, M.; Wang, X.D.; Zhang, T. Hexaaluminates: A review of the structure, synthesis and catalytic performance. *Catal. Sci. Technol.* **2016**, *6*, 1984–2004. [CrossRef]
59. Yang, J.; Guo, Y. Nanostructured perovskite oxides as promising substitutes of noble metals catalysts for catalytic combustion of methane. *Chin. Chem. Lett.* **2018**, *29*, 252–260. [CrossRef]
60. Cargnello, M.; Delgado Jaén, J.J.; Hernández Garrido, J.C.; Bakhmutsky, K.; Montini, T.; Calvino Gámez, J.J.; Gorte, R.J.; Fornasiero, P. Exceptional activity for methane combustion over modular $Pd@CeO_2$ subunits on functionalized Al_2O_3. *Science* **2012**, *337*, 713–717. [CrossRef] [PubMed]
61. Florén, C.-R.; Demirci, C.; Carlsson, P.-A.; Creaser, D.; Skoglundh, M. Total oxidation of methane over Pd/Al2O3 at pressures from 1 to 10 atm. *Catal. Sci. Technol.* **2020**, *10*, 5480–5486. [CrossRef]
62. Wang, Y.; Arandiyan, H.; Scott, J.; Akia, M.; Dai, H.; Deng, J.; Aguey-Zinsou, K.-F.; Amal, R. High Performance Au–Pd Supported on 3D Hybrid Strontium-Substituted Lanthanum Manganite Perovskite Catalyst for Methane Combustion. *ACS Catal.* **2016**, *6*, 6935–6947. [CrossRef]
63. Li, X.; Liu, Y.; Deng, J.; Zhang, Y.; Xie, S.; Zhao, X.; Wang, Z.; Guo, G.; Dai, H. 3DOM $LaMnAl_{11}O_{19}$-supported AuPd alloy nanoparticles: Highly active catalysts for methane combustion in a continuous-flow microreactor. *Catal. Today* **2018**, *308*, 71–80. [CrossRef]
64. Arandiyan, H.; Dai, H.; Ji, K.; Sun, H.; Li, J. Pt Nanoparticles Embedded in Colloidal Crystal Template Derived 3D Ordered Macroporous $Ce_{0.6}Zr_{0.3}Y_{0.1}O_2$: Highly Efficient Catalysts for Methane Combustion. *ACS Catal.* **2015**, *5*, 1781–1793. [CrossRef]
65. Jones, J.M.; Dupont, V.A.; Brydson, R.; Fullerton, D.J.; Nasri, N.S.; Ross, A.B.; Westwood, A.V.K. Sulphur poisoning and regeneration of precious metal catalysed methane combustion. *Catal. Today* **2003**, *81*, 589–601. [CrossRef]
66. Liu, Y.; Zheng, H.; Liu, J.; Zhang, T. Preparation of high surface area $La_{1-x}A_xMnO_3$ (A=Ba, Sr or Ca) ultra-fine particles used for CH4 oxidation. *Chem. Eng. J.* **2002**, *89*, 213–221. [CrossRef]
67. Rossetti, I.; Buchneva, O.; Biffi, C.; Rizza, R. Effect of sulphur poisoning on perovskite catalysts prepared by flame-pyrolysis. *Appl. Catal. B Environ.* **2009**, *89*, 383–390. [CrossRef]
68. Du, X.; Zou, G.; Zhang, Y.; Wang, X. A novel strategy for low-temperature synthesis of Ruddlesden–Popper type layered perovskite $La_3Mn_2O_{7+\delta}$ for methane combustion. *J. Mater. Chem. A* **2013**, *1*, 8411–8416. [CrossRef]
69. Wang, Y.; Arandiyan, H.; Tahini, H.A.; Scott, J.; Tan, X.; Dai, H.; Gale, J.D.; Rohl, A.L.; Smith, S.C.; Amal, R. The controlled disassembly of mesostructured perovskites as an avenue to fabricating high performance nanohybrid catalysts. *Nat. Commun.* **2017**, *8*, 15553. [CrossRef] [PubMed]
70. Ren, Z.; Botu, V.; Wang, S.; Meng, Y.; Song, W.; Guo, Y.; Ramprasad, R.; Suib, S.L.; Gao, P.X. Monolithically Integrated Spinel $M_xCo_{3-x}O_4$ (M=Co, Ni, Zn) Nanoarray Catalysts: Scalable Synthesis and Cation Manipulation for Tunable Low-Temperature CH_4 and CO Oxidation. *Angew. Chem. Int. Ed.* **2014**, *53*, 7223–7227. [CrossRef] [PubMed]
71. Shan, W. Reduction property and catalytic activity of $Ce_{1-X}Ni_XO_2$ mixed oxide catalysts for CH_4 oxidation. *Appl. Catal. A Gen.* **2003**, *246*, 1–9. [CrossRef]
72. Li, J.; Liang, X.; Xu, S.; Hao, J. Catalytic performance of manganese cobalt oxides on methane combustion at low temperature. *Appl. Catal. B Environ.* **2009**, *90*, 307–312. [CrossRef]
73. Choya, A.; de Rivas, B.; González-Velasco, J.R.; Gutiérrez-Ortiz, J.I.; López-Fonseca, R. Oxidation of residual methane from VNG vehicles over Co_3O_4-based catalysts: Comparison among bulk, Al_2O_3-supported and Ce-doped catalysts. *Appl. Catal. B Environ.* **2018**, *237*, 844–854. [CrossRef]

74. Zhang, Y.; Qin, Z.; Wang, G.; Zhu, H.; Dong, M.; Li, S.; Wu, Z.; Li, Z.; Wu, Z.; Zhang, J.; et al. Catalytic performance of MnO_x–NiO composite oxide in lean methane combustion at low temperature. *Appl. Catal. B Environ.* **2013**, *129*, 172–181. [CrossRef]
75. Yu, Q.; Wang, C.; Li, X.; Li, Z.; Wang, L.; Zhang, Q.; Wu, G.; Li, Z. Engineering an effective MnO_2 catalyst from $LaMnO_3$ for catalytic methane combustion. *Fuel* **2019**, *239*, 1240–1245. [CrossRef]
76. Wang, X.; Liu, Y.; Zhang, Y.; Zhang, T.; Chang, H.; Zhang, Y.; Jiang, L. Structural requirements of manganese oxides for methane oxidation: XAS spectroscopy and transition-state studies. *Appl. Catal. B Environ.* **2018**, *229*, 52–62. [CrossRef]
77. Rhodes, C.J. Endangered elements, critical raw materials and conflict minerals. *Sci. Prog.* **2019**, *102*, 304–350. [CrossRef] [PubMed]
78. Biswal, A.; Chandra Tripathy, B.; Sanjay, K.; Subbaiah, T.; Minakshi, M. Electrolytic manganese dioxide (EMD): A perspective on worldwide production, reserves and its role in electrochemistry. *RSC Adv.* **2015**, *5*, 58255–58283. [CrossRef]
79. Ji, X.; Xia, Q.; Xu, Y.; Feng, H.; Wang, P.; Tan, Q. A review on progress of lithium-rich manganese-based cathodes for lithium ion batteries. *J. Power Sources* **2021**, *487*, 229362. [CrossRef]
80. Euro Manganese Sees Spike in EV Battery Maker Demand by 2030. Available online: https://www.marketindex.com.au/news/euro-manganese-sees-spike-in-ev-battery-maker-demand-by-2030 (accessed on 30 September 2022).
81. Zhanpeisov, N. Cluster quantum-chemical study of the chemisorption of methane on zinc oxide surface. *J. Mol. Catal. A Chem.* **1995**, *99*, 35–39. [CrossRef]
82. Yang, J.; Xiao, W.; Chi, X.; Lu, X.; Hu, S.; Wu, Z.; Tang, W.; Ren, Z.; Wang, S.; Yu, X.; et al. Solar-driven efficient methane catalytic oxidation over epitaxial ZnO/La0.8Sr0.2CoO3 heterojunctions. *Appl. Catal. B Environ.* **2020**, *265*, 118469. [CrossRef]
83. Wang, S.; Ren, Z.; Song, W.; Guo, Y.; Zhang, M.; Suib, S.L.; Gao, P.-X. ZnO/perovskite core–shell nanorod array based monolithic catalysts with enhanced propane oxidation and material utilization efficiency at low temperature. *Catal. Today* **2015**, *258*, 549–555. [CrossRef]
84. Chen, L.-J.; Chuang, Y.-J. Hydrothermal synthesis and characterization of hexagonal zinc oxide nanorods with a hexamethylenetetramine (HMTA) template-assisted at a low temperature. *Mater. Lett.* **2012**, *68*, 460–462. [CrossRef]
85. Biswas, K.; Das, B.; Rao, C.N.R. Growth Kinetics of ZnO Nanorods: Capping-Dependent Mechanism and Other Interesting Features. *J. Phys. Chem. C* **2008**, *112*, 2404–2411. [CrossRef]
86. Rayathulhan, R.; Sodipo, B.K.; Aziz, A.A. Nucleation and growth of zinc oxide nanorods directly on metal wire by sonochemical method. *Ultrason. Sonochem.* **2017**, *35*, 270–275. [CrossRef] [PubMed]
87. Leontiou, A.A.; Ladavos, A.K.; Giannakas, A.E.; Bakas, T.V.; Pomonis, P.J. A comparative study of substituted perovskite-type solids of oxidic $La_{1-x}Sr_xFeO_{3\pm\delta}$ and chlorinated $La_{1-x}Sr_xFeO_{3\pm\delta}Cl_\sigma$ form: Catalytic performance for CH_4 oxidation by O_2 or N_2O. *J. Catal.* **2007**, *251*, 103–112. [CrossRef]
88. Najjar, H.; Batis, H.; Lamonier, J.-F.; Mentré, O.; Giraudon, J.-M. Effect of praseodymium and europium doping in $La_{1-x}Ln_xMnO_{3\pm\delta}$ (Ln: Pr or Eu, $0 \leq x \leq 1$) perosvkite catalysts for total methane oxidation. *Appl. Catal. A Gen.* **2014**, *469*, 98–107. [CrossRef]
89. Valdez, C.N.; Delley, M.F.; Mayer, J.M. Cation Effects on the Reduction of Colloidal ZnO Nanocrystals. *J. Am. Chem. Soc.* **2018**, *140*, 8924–8933. [CrossRef] [PubMed]
90. Ye, H.; Na, W.; Gao, W.; Wang, H. Carbon-Modified CuO/ZnO Catalyst with High Oxygen Vacancy for CO_2 Hydrogenation to Methanol. *Energy Technol.* **2020**, *8*, 2000194. [CrossRef]
91. Wang, W.; Xie, Y.; Zhang, S.; Liu, X.; Haruta, M.; Huang, J. Selective Hydrogenation of Cinnamaldehyde Catalyzed by ZnO-Fe_2O_3 Mixed Oxide Supported Gold Nanocatalysts. *Catalysts* **2018**, *8*, 60. [CrossRef]
92. Wang, W.; Li, X.; Zhang, Y.; Zhang, R.; Ge, H.; Bi, J.; Tang, M. Strong metal–support interactions between Ni and ZnO particles and their effect on the methanation performance of Ni/ZnO. *Catal. Sci. Technol.* **2017**, *7*, 4413–4421. [CrossRef]
93. Lv, Y.; Yao, W.; Ma, X.; Pan, C.; Zong, R.; Zhu, Y. The surface oxygen vacancy induced visible activity and enhanced UV activity of a ZnO1−x photocatalyst. *Catal. Sci. Technol.* **2013**, *3*, 3136–3146. [CrossRef]
94. Han, X.-G.; He, H.-Z.; Kuang, Q.; Zhou, X.; Zhang, X.-H.; Xu, T.; Xie, Z.-X.; Zheng, L.-S. Controlling Morphologies and Tuning the Related Properties of Nano/Microstructured ZnO Crystallites. *J. Phys. Chem. C* **2008**, *113*, 584–589. [CrossRef]
95. Zhao, L.; Zhang, Y.; Bi, S.; Liu, Q. Metal–organic framework-derived CeO_2–ZnO catalysts for C_3H_6-SCR of NO: An in situ DRIFTS study. *RSC Adv.* **2019**, *9*, 19236–19242. [CrossRef] [PubMed]
96. De Siqueira, R.N.C.; de Albuquerque Brocchi, E.; de Oliveira, P.F.; Motta, M.S. Hydrogen Reduction of Zinc and Iron Oxides Containing Mixtures. *Metall. Mater. Trans. B* **2013**, *45*, 66–75. [CrossRef]
97. Maity, N.; Barman, S.; Minenkov, Y.; Ould-Chikh, S.; Abou-Hamad, E.; Ma, T.; Qureshi, Z.S.; Cavallo, L.; D'Elia, V.; Gates, B.C.; et al. A Silica-Supported Monoalkylated Tungsten Dioxo Complex Catalyst for Olefin Metathesis. *ACS Catal.* **2018**, *8*, 2715–2729. [CrossRef]
98. Song, S.; Song, H.; Li, L.; Wang, S.; Chu, W.; Peng, K.; Meng, X.; Wang, Q.; Deng, B.; Liu, Q.; et al. A selective Au-ZnO/TiO_2 hybrid photocatalyst for oxidative coupling of methane to ethane with dioxygen. *Nat. Catal.* **2021**, *4*, 1032–1042. [CrossRef]
99. Sun, Y.; Xu, J.; Xu, X.; Fang, X.; Guo, Y.; Liu, R.; Zhong, W.; Wang, X. Tailoring Active O_2^- and O_2^{2-} Anions on a ZnO Surface with the Addition of Different Alkali Metals Probed by CO Oxidation. *Ind. Eng. Chem. Res.* **2020**, *59*, 9382–9392. [CrossRef]
100. Najjar, H.; Lamonier, J.-F.; Mentré, O.; Giraudon, J.-M.; Batis, H. Combustion synthesis of $LaMn_{1-x}Al_xO_{3+\delta}$ ($0 \leq x \leq 1$): Tuning catalytic properties for methane deep oxidation. *Catal. Sci. Technol.* **2013**, *3*, 1002–1016. [CrossRef]
101. Ferri, D.; Forni, L. Methane combustion on some perovskite-like mixed oxides. *Appl. Catal. B Environ.* **1998**, *16*, 119–126. [CrossRef]

102. Zhou, J.; Nomenyo, K.; Cesar, C.C.; Lusson, A.; Schwartzberg, A.; Yen, C.-C.; Woon, W.-Y.; Lerondel, G. Giant defect emission enhancement from ZnO nanowires through desulfurization process. *Sci. Rep.* **2020**, *10*, 4237. [CrossRef] [PubMed]
103. Uklein, A.V.; Multian, V.V.; Kuz'micheva, G.M.; Linnik, R.P.; Lisnyak, V.V.; Popov, A.I.; Gayvoronsky, V.Y. Nonlinear optical response of bulk ZnO crystals with different content of intrinsic defects. *Opt. Mater.* **2018**, *84*, 738–747. [CrossRef]
104. Brik, M.G.; Srivastava, A.M.; Popov, A.I. A few common misconceptions in the interpretation of experimental spectroscopic data. *Opt. Mater.* **2022**, *127*, 112276. [CrossRef]
105. Panigrahy, B.; Aslam, M.; Misra, D.S.; Ghosh, M.; Bahadur, D. Defect-Related Emissions and Magnetization Properties of ZnO Nanorods. *Adv. Funct. Mater.* **2010**, *20*, 1161–1165. [CrossRef]
106. Chen, D.; Wang, Z.; Ren, T.; Ding, H.; Yao, W.; Zong, R.; Zhu, Y. Influence of Defects on the Photocatalytic Activity of ZnO. *J. Phys. Chem. C* **2014**, *118*, 15300–15307. [CrossRef]
107. Liu, Y.; Peng, Y.; Naschitzki, M.; Gewinner, S.; Schöllkopf, W.; Kuhlenbeck, H.; Pentcheva, R.; Roldan Cuenya, B. Surface oxygen Vacancies on Reduced Co3O4 (100): Superoxide Formation and Ultra-Low-Temperature CO Oxidation. *Angew. Chem. Int. Ed.* **2021**, *60*, 16514–16520. [CrossRef] [PubMed]
108. Sun, Y.; Liu, J.; Song, J.; Huang, S.; Yang, N.; Zhang, J.; Sun, Y.; Zhu, Y. Exploring the Effect of Co_3O_4 Nanocatalysts with Different Dimensional Architectures on Methane Combustion. *ChemCatChem* **2016**, *8*, 540–545. [CrossRef]
109. Gurlo, A. Interplay between O_2 and SnO_2: Oxygen Ionosorption and Spectroscopic Evidence for Adsorbed Oxygen. *ChemPhysChem* **2006**, *7*, 2041–2052. [CrossRef]
110. Anpo, M.; Costentin, G.; Giamello, E.; Lauron-Pernot, H.; Sojka, Z. Characterisation and reactivity of oxygen species at the surface of metal oxides. *J. Catal.* **2021**, *393*, 259–280. [CrossRef]
111. Liang, S.; Teng, F.; Bulgan, G.; Zhu, Y. Effect of Jahn−Teller Distortion in $La_{0.5}Sr_{0.5}MnO_3$ Cubes and Nanoparticles on the Catalytic Oxidation of CO and CH_4. *J. Phys. Chem. C* **2007**, *111*, 16742–16749. [CrossRef]
112. Gandla, S.; Gollu, S.R.; Sharma, R.; Sarangi, V.; Gupta, D. Dual role of boron in improving electrical performance and device stability of low temperature solution processed ZnO thin film transistors. *Appl. Phys. Lett.* **2015**, *107*, 152012. [CrossRef]
113. Fan, X.; Li, L.; Jing, F.; Li, J.; Chu, W. Effects of preparation methods on $CoAlO_x/CeO_2$ catalysts for methane catalytic combustion. *Fuel* **2018**, *225*, 588–595. [CrossRef]
114. Zhong, L.; Fang, Q.; Li, X.; Li, Q.; Zhang, C.; Chen, G. Influence of preparation methods on the physicochemical properties and catalytic performance of Mn-Ce catalysts for lean methane combustion. *Appl. Catal. A Gen.* **2019**, *579*, 151–158. [CrossRef]
115. Arandiyan, H.; Chang, H.; Liu, C.; Peng, Y.; Li, J. Dextrose-aided hydrothermal preparation with large surface area on 1D single-crystalline perovskite $La_{0.5}Sr_{0.5}CoO_3$ nanowires without template: Highly catalytic activity for methane combustion. *J. Mol. Catal. A Chem.* **2013**, *378*, 299–306. [CrossRef]
116. Ding, Y.; Wang, S.; Zhang, L.; Chen, Z.; Wang, M.; Wang, S. A facile method to promote $LaMnO_3$ perovskite catalyst for combustion of methane. *Catal. Commun.* **2017**, *97*, 88–92. [CrossRef]
117. Pecchi, G.; Jiliberto, M.G.; Buljan, A.; Delgado, E.J. Relation between defects and catalytic activity of calcium doped $LaFeO_3$ perovskite. *Solid State Ion.* **2011**, *187*, 27–32. [CrossRef]
118. Arandiyan, H.; Dai, H.; Deng, J.; Liu, Y.; Bai, B.; Wang, Y.; Li, X.; Xie, S.; Li, J. Three-dimensionally ordered macroporous La0.6Sr0.4MnO3 with high surface areas: Active catalysts for the combustion of methane. *J. Catal.* **2013**, *307*, 327–339. [CrossRef]
119. Arandiyan, H.; Dai, H.; Deng, J.; Wang, Y.; Sun, H.; Xie, S.; Bai, B.; Liu, Y.; Ji, K.; Li, J. Three-Dimensionally Ordered Macroporous La0.6Sr0.4MnO3 Supported Ag Nanoparticles for the Combustion of Methane. *J. Phys. Chem. C* **2014**, *118*, 14913–14928. [CrossRef]
120. Taguchi, H.; Nakade, K.; Yosinaga, M.; Kato, M.; Hirota, K. Methane Oxidation on Perovskite-Type $Ca(Mn_{1-x}Ti_x)O_{3-\delta}$. *J. Am. Ceram. Soc.* **2007**, *91*, 308–310. [CrossRef]
121. Li, H.; Lu, G.; Qiao, D.; Wang, Y.; Guo, Y.; Guo, Y. Catalytic Methane Combustion over Co_3O_4/CeO_2 Composite Oxides Prepared by Modified Citrate Sol–Gel Method. *Catal. Lett.* **2010**, *141*, 452–458. [CrossRef]
122. Gao, Q.-X.; Wang, X.-F.; Di, J.-L.; Wu, X.-C.; Tao, Y.-R. Enhanced catalytic activity of α-Fe_2O_3 nanorods enclosed with {110} and {001} planes for methane combustion and CO oxidation. *Catal. Sci. Technol.* **2011**, *1*, 574–577. [CrossRef]
123. Gao, Q.-X.; Wang, X.-F.; Wu, X.-C.; Tao, Y.-R.; Zhu, J.-J. Mesoporous zirconia nanobelts: Preparation, characterization and applications in catalytical methane combustion. *Microporous Mesoporous Mater.* **2011**, *143*, 333–340. [CrossRef]
124. Chen, J.; Shi, W.; Zhang, X.; Arandiyan, H.; Li, D.; Li, J. Roles of Li^+ and Zr^{4+} Cations in the Catalytic Performances of $Co_{1-x}M_xCr_2O_4$ (M = Li, Zr; x = 0–0.2) for Methane Combustion. *Environ. Sci. Technol.* **2011**, *45*, 8491–8497. [CrossRef] [PubMed]
125. Zhang, C.C.; Hartlaub, S.; Petrovic, I.; Yilmaz, B. Raman Spectroscopy Characterization of Amorphous Coke Generated in Industrial Processes. *ACS Omega* **2022**, *7*, 2565–2570. [CrossRef] [PubMed]
126. Vogelaar, B.M.; van Langeveld, A.D.; Eijsbouts, S.; Moulijn, J.A. Analysis of coke deposition profiles in commercial spent hydroprocessing catalysts using Raman spectroscopy. *Fuel* **2007**, *86*, 1122–1129. [CrossRef]
127. Daumann, S.; Andrzejewski, D.; Di Marcantonio, M.; Hagemann, U.; Wepfer, S.; Vollkommer, F.; Bacher, G.; Epple, M.; Nannen, E. Water-free synthesis of ZnO quantum dots for application as an electron injection layer in light-emitting electrochemical cells. *J. Mater. Chem. C* **2017**, *5*, 2344–2351. [CrossRef]
128. Ahmad, M.Z.; Chang, J.; Ahmad, M.S.; Waclawik, E.R.; Wlodarski, W. Non-aqueous synthesis of hexagonal ZnO nanopyramids: Gas sensing properties. *Sens. Actuators B Chem.* **2013**, *177*, 286–294. [CrossRef]

129. Li, Y.; Luo, C.; Liu, Z.; Lin, F. Experimental Study on Catalytic Combustion of Methane in a Microcombustor with Metal Foam Monolithic Catalyst. *Catalysts* **2018**, *8*, 536. [CrossRef]
130. Wierzbicki, T.A.; Lee, I.C.; Gupta, A.K. Rh assisted catalytic oxidation of jet fuel surrogates in a meso-scale combustor. *Appl. Energy* **2015**, *145*, 1–7. [CrossRef]